INTEGRAL TWIST ACTUATION OF HELICOPTER ROTOR BLADES FOR VIBRATION REDUCTION

SangJoon Shin
Carlos E. S. Cesnik

August 2001 AMSL # 01-07

This report is based on the thesis of SangJoon Shin submitted to the Department of Aeronautics and Astronautics in partial fulfillment of the requirements for the degree of Doctor of Philosophy at the Massachusetts Institute of Technology.

(Under the sponsorship of NASA)

ABSTRACT

Active integral twist control for vibration reduction of helicopter rotors during forward flight is investigated. The twist deformation is obtained using embedded anisotropic piezocomposite actuators. An analytical framework is developed to examine integrally-twisted blades and their aeroelastic response during different flight conditions: frequency domain analysis for hover, and time domain analysis for forward flight. Both stem from the same three-dimensional electroelastic beam formulation with geometrical-exactness, and are coupled with a finite-state dynamic inflow aerodynamics model. A prototype Active Twist Rotor blade was designed with this framework using Active Fiber Composites as the actuator. The ATR prototype blade was successfully tested under non-rotating conditions. Hover testing was conducted to evaluate structural integrity and dynamic response. In both conditions, a very good correlation was obtained against the analysis. Finally, a four-bladed ATR system is built and tested to demonstrate its concept in forward flight. This experiment was conducted at NASA Langley Transonic Dynamics Tunnel and represents the first-of-a-kind Mach-scaled fully-active-twist rotor system to undergo forward flight test. In parallel, the impact upon the fixed- and rotating-system loads is estimated by the analysis. While discrepancies are found in the amplitude of the loads under actuation, the predicted trend of load variation with respect to its control phase correlates well. It was also shown, both experimentally and numerically, that the ATR blade design has the potential for hub vibratory load reduction of up to 90% using individual blade control actuation. Using the numerical framework, system identification is performed to estimate the harmonic transfer functions. The linear time-periodic system can be represented by a linear time-invariant system under the three modes of blade actuation: collective, longitudinal cyclic, and lateral cyclic. A vibration minimizing controller is designed based on this result, which implements classical disturbance rejection algorithm with some modifications. The controller is simulated numerically, and more than 90% of the 4P hub vibratory load is eliminated.

By accomplishing the experimental and analytical steps described in this thesis, the present concept is found to be a viable candidate for future generation low-vibration helicopters. Also, the analytical framework is shown to be very appropriate for exploring active blade designs, aeroelastic behavior prediction, and as simulation tool for closed-loop controllers.

Acknowledgments

This work was supported by the U.S. Army Research Laboratory, at NASA Langley Research Center under the cooperative agreement # NCC1-323, with Mr. Matthew L. Wilbur serving as a technical monitor.

Contents

1 Introduction **27**

1.1 Background 27

1.2 Helicopter Vibration Reduction 29

1.3 Previous Work Related with Integral Twist Actuation 31

1.3.1 Actuators Applicable for the Integral Concept 31

1.3.2 Previous Integral Helicopter Blades 32

1.3.3 ATR Blade – Previous Work 33

1.4 Present Work 35

2 Analytical Framework **39**

2.1 Introduction 39

2.2 Cross-Sectional Analysis 42

2.3 Global Beam Analysis 45

2.3.1 Mixed Form for Hover Analysis 45

2.3.2 Displacement-based Form for Forward Flight Analysis 50

2.4 Aerodynamic Analysis 53

2.4.1 Hover Aerodynamics 53

2.4.2 Forward Flight Aerodynamics 55

2.5 Solution of the Aeroelastic System 56

2.5.1 Frequency Domain Solution for Hover Analysis 56

2.5.2 Time Domain Solution for Forward Flight Analysis 59

5.4 Correlation of Forward Flight Analyses with Experiments 113

6 System Identification of the ATR System in Forward Flight 115

6.1 Overview 115

6.2 Input Signals for System Identification 116

6.3 Results of the ATR System Identification 119

6.3.1 Collective Mode of Actuation 119

6.3.2 Cyclic Mode of Actuation 124

7 Closed-loop Controller for Vibration Reduction in Forward Flight 127

7.1 Overview 127

7.2 LTI Feedback Compensator for Disturbance Rejection 128

7.3 Stability of the Closed-loop System 130

7.3.1 Original Feedback Controller 130

7.3.2 Modified Feedback Controller 133

7.4 Numerical Demonstration of the Closed-loop Controller 134

8 Conclusions and Recommendations 139

8.1 Summary 139

8.2 Conclusions 141

8.3 Recommendations 142

A State-space Formulation for Hover Analysis 145

B Time Integration Formulation for Forward Flight Analysis 147

C AFC Distribution in the ATR Prototype Blade 149

D Material Properties of the ATR Test Blade Constituents 151

E LTP System and its Identification 153

E.1 Characteristics of LTP system 153

E.2 Identification Methodology of the LTP System 156

E.3 Implementation of the Developed Methodology 160

List of Figures

1-1 Aerodynamic environment in forward flight [3] 28

1-2 AFC being inserted at active blade assembly 32

1-3 MFC actuator 32

1-4 Overview of different stages of the NASA/Army/MIT ATR program . 36

2-1 Schematic diagram of the analytical framework for an active helicopter blade and its aeroelastic behavior 40

2-2 Two-cell thin-walled cross section beam 43

2-3 Degradation of free strain actuation with the frequency of excitation for the piezoelectric actuators used in the ATR blade 44

2-4 Blade frames of reference for the global analysis 46

2-5 Beam in the undeformed and deformed configurations 51

3-1 Planform and cross-section of the ATR prototype blade (Dimensions are in inches.) 63

3-2 Fan plot of the ATR prototype blade from the proposed analysis . . . 63

3-3 ATR prototype blade 67

3-4 The Langley Transonic Dynamic Tunnel (TDT) [48] 68

3-5 Schematic of the Aeroelastic Rotor Experimental System (ARES) helicopter testbed (All dimensions are in ft.) [48] 69

3-6 Aeroelastic Rotor Experimental System (ARES) 9-ft diameter rotor testbed in Langley Transonic Dynamic Tunnel (TDT) with the ATR prototype blade. 70

5-3 Equivalent torsional moment at 49% blade radius of the ATR blade at bench 90
5-4 Detailed multi-body representation of 4-active-bladed ATR system . . 91
5-5 Example of high-voltage input generated for an IBC-mode 3P actuation with 12 divisions of control phase angle 93
5-6 Azimuthal locations where the maximum amplitude occurs for the first two actuation periods during the 3P actuation input generated in Fig. 5-5 94
5-7 Simulated time history of hub vertical shear forces when the 3P actuation is applied as described in Fig. 5-5 95
5-8 Variation of 4P hub shear vibratory loads for $\mu = 0.140$, $\alpha_S = -1°$, $C_T = 0.0066$, and 1,000 V twist actuation at 3P, 4P, 5P with respect to control phase 96
5-9 Variation of flap bending moment at 28.7% span location for $\mu = 0.140$, $\alpha_S = -1°$, $C_T = 0.0066$, and 1,000 V twist actuation at 3P, 4P, 5P with respect to control phase 98
5-10 Variation of torsional moment at 33.6% span location for $\mu = 0.140$, $\alpha_S = -1°$, $C_T = 0.0066$, and 1,000 V twist actuation at 3P, 4P, 5P with respect to control phase 99
5-11 Polar plot of 4P hub shear vibratory loads for $\mu = 0.140$, $\alpha_S = -1°$, $C_T = 0.0066$, and 1,000 V twist actuation at 3P, compared with the baseline value 101
5-12 Variation of 4P hub shear vibratory loads for $\mu = 0.333$, $\alpha_S = -6°$, $C_T = 0.0066$, and 1,000 V twist actuation at 3P, 4P, 5P with respect to control phase 103
5-13 Variation of flap bending moment at 28.7% span location for $\mu = 0.333$, $\alpha_S = -6°$, $C_T = 0.0066$, and 1,000 V twist actuation at 3P, 4P, 5P with respect to control phase 104

6-5 Component remaining from the original response after subtracting the one represented by G_0 122
6-6 Harmonic transfer function G_0 of the hub vertical shear loads during the collective mode actuation 123
6-7 Polar plot of 4P hub vertical shear loads variation during 4P sine-dwell actuation 124
6-8 Matrix of G_0 estimated for three components of 4P hub shear vibratory loads versus three modes of blade actuation 125

7-1 Block diagram of the higher harmonic control system adopted by researchers using quasisteady helicopter plant model [9] 129
7-2 Block diagram of the LTI feedback compensator equivalent to HHC algorithm for vibration rejection [9] 130
7-3 Bode plot of the loop transfer function 131
7-4 Nichols plot of the loop transfer function 132
7-5 Time history of the hub vertical shear loads for $\mu = 0.140$, $\alpha_S = -1°$, and $C_T = 0.0066$ without and with the closed-loop controller engaged 136
7-6 Power spectral desnity distribution of the hub vertical shear loads for $\mu = 0.140$, $\alpha_S = -1°$, and $C_T = 0.0066$ without and with the closed-loop controller engaged 137

E-1 LTP system block diagram with three transfer functions [62] 157
E-2 Input signals generated with appropriate time intervals over the system period [62] 158
E-3 Delayed input signal and corresponding output of LTP system [62] . . 159

List of Tables

3.1 General properties of the existing baseline rotor blade (considering heavy gas test medium) 62

3.2 Theoretical characteristics of the ATR prototype design 64

3.3 Basic characteristics of the modified ATR blade design 66

3.4 Hover test conditions for the ATR prototype blade 71

3.5 Data channels for the hover test. 72

3.6 Forward flight test conditions for the ATR system 73

4.1 Peak-to-peak tip twist actuation of the ATR prototype blade (2,000 V_{pp}/0 V_{DC}, 1 Hz) 77

5.1 Trim control inputs for the forward flight test conditions 91

5.2 Geometry and material property of the upgraded ATR system model 107

5.3 Fixed-system baseline loads predicted with different blade structural representations and c.g. locations ($\mu = 0.140$, $\alpha_S = -1°$, $C_T = 0.0066$) 114

C.1 Active properties of the AFC packs distributed in the ATR prototype blade (pm/V) 150

D.1 Material properties of the constituents in the ATR test blades 151

D.2 Properties of the AFC packs used in the ATR test blades 152

Nomenclature

a	lift curve slope of the airfoil
$\mathbf{a}$	global frame attached to the hub
$\mathbf{a}_o$	conformal rotation vector of the rotation from B_n^- to B_{n+1}^-, measured in the $\mathbf{a}$ frame
$\mathcal{A}$	dynamics matrix in harmonic state-space formulation
$A(t)$	dynamics matrix in state-space formulation
b	number of blades
$\mathbf{b}$	undeformed reference frame of the blade
$\mathbf{b}_o$	conformal rotation vector of the rotation from B_n^- to B_n^+, measured in the $\mathbf{a}$ frame
$\mathbf{B}$	deformed reference frame of the blade
$\mathcal{B}$	input matrix in harmonic state-space formulation
$B(t)$	input matrix in state-space formulation
c	blade chord length
c_{d_o}	profile drag coefficient of the airfoil
C^{ba}	transformation matrix from a to b
C^{Ba}	transformation matrix from a to B
C	rotation matrix, product of C^{ab} and C^{Ba}
$\mathcal{C}$	output matrix (related to state vector) in harmonic state-space formulation
$C(t)$	output matrix (related to state vector) in state-space formulation
C_T	non-dimensionalized rotor thrust coefficient

$\mathcal{G}$	harmonic transfer function
h	thickness of the shell surface
H_B	angular momentum column vector
I	3×3 inertial matrix
$\mathbf{k}$	sectional elastic curvature vector
J	cost function
K	kinetic energy density per unit span of the blade
$[K]$	general 6×6 stiffness matrix
$K(s)$	transfer function of the feedback compensator
K_B	sectional stiffness matrix measured in the **B** frame
K_{ij}	beam stiffness components
L	length of the shell
m	blade mass per unit span length
m_a	external moment vector
M_1	beam torsional moment
$M_2,\ M_3$	beam bending moments
$M_1^{(a)}$	actuation component of beam torsional moment
$M_2^{(a)},\ M_3^{(a)}$	actuation components of beam bending moments
M_B	internal moment column vector in the **B** frame
$M_B^{(a)}$	actuation column vector for internal moment
M_{dB}	column vector of the viscous moments in the **B** frame
n	number of data points in input vector $\mathbf{u}$
n_c	number of chirps that have already been generated
n_h	number of harmonic transfer functions to be evaluated
N	number of the one-dimensional elements for blade spanwise discretization
N	number of chirp to be generated in input signal
$\mathcal{N}$	frequency modulation (block diagonal) matrix
$\mathbf{p}_B$	sectional momentum vector measured in the **B** frame

$u_i,\ \theta_i,\ F_i$	constant vectors of the corresponding quantities at each
$M_i,\ P_i,\ H_i$	node i
U	potential energy density per unit span of the blade
$U(j\omega)$	input matrix with elements in frequency domain
$\mathbf{U}$	matrix with modulated and Fourier transformed input data vector elements
$\mathbf{U_c}$	chirp input vector for rotor system
$v_1,\ v_s,\ v_\xi$	displacement field of an arbitrary point in the shell frame
$v_1^{(a)}(s)$	actuation contribution to the out-of-plane displacement
V	magnitude of the electric field distribution shape
$\mathbf{V}$	vector for rotor actuation mode selection
V_B	linear velocity column vector in the **B** frame
w_a	initial angular velocity of a generic point on the **a** frame
$W_{B2},\ W_{B3}$	component of the relative wind velocity in the **B** frame
$\overline{\delta W}$	virtual work of applied loads per unit span
x	beam axial coordinate
$x(t)$	state vector in state-space formulation
X	column matrix of the structural variables in one-dimensional beam formulation
$\mathcal{X}$	harmonic state vector
$\bar{X}$	steady components of the structural variables X
$\check{X}(t)$	perturbed motion components of the structural variables X
y	output vector in the state space representation of the beam
$y,\ z$	Cartesian coordinates with respect to the reference point in the cross section
$\mathbf{y}$	vector of discretized $y(t)$
$y(t)$	output signal in time domain
Y	column matrix of the inflow state variables in one-dimensional beam formulation

θ_o	collective pitch angle setting
ρ	weight density of the blade
ρ_∞	air mass density
ω	input frequency to excite the system
$\boldsymbol{\omega}$	sectional angular velocity vector
ω_p	major frequency of the system
Ω	rotor rotational frequency
Ω_1	component of the blade rotation speed along $\mathbf{B}_1$ direction
Ω_B	angular velocity column vector in the $\mathbf{B}$ frame
Ω_o	nominal rotational speed of the rotor system
ξ	local coordinate of each beam finite element
ψ	blade azimuth angle
$\boldsymbol{\psi}$	vector of azimuthal locations
$\bar{\psi}$	azimuthal location of the blade in the rotating frame
$\dot{(\,)}$, $(\,)^\bullet$	derivative with respect to time
$(\,)'$	derivative with respect to the beam span coordinate, x_1
$(\,)^*$	geometrically-exact kinematical quantity in the $\mathbf{a}$ frame
$\hat{(\,)}$	boundary values of the corresponding quantities
$\tilde{(\,)}$	skew-symmetric matrix

Chapter 1

Introduction

1.1 Background

Rotorcraft has been a very important mode of aerial transportation due to its capability of vertical take-off and landing, enabling many unique missions such as rescue operation at sea. However, it has also been under several serious constraints such as poor ride quality due to high levels of vibration [1] and noise, restricted flight envelope, low fatigue life of the structural components, and high operating cost. The primary source of those problems is the complex unsteady aerodynamic environment which is generated near the rotor blades mainly during forward flight [2]. An instantaneous asymmetry of the aerodynamic loads acting on the blades at different azimuth location is developed, and such asymmetry becomes more and more adverse as the forward flight speed increases. Therefore, the rotor system is the major component from which helicopter vibrations originate, and the resulting vibratory load becomes a dominant factor of reducing the life of fatigue-critical components and poor ride quality. These vibrations also limit the performance of the helicopters such as forward flight speeds, and tend to decrease payload due to the addition of extra vibration-alleviation devices. The coupling between the structural and mechanical components such as rotor, fuselage, engine, and transmission adds another degree of complexity to this problem.

A typical aerodynamic environment of the helicopter main rotor during forward

vibrations.

1.2 Helicopter Vibration Reduction

There have been considerable efforts to reduce the vibration in helicopter [4, 5], and vibration alleviation methodologies employed by the helicopter designers may be categorized into the following three groups:

1. Varying passive structural properties of the rotor system or fuselage by tuning its dynamic characteristics [6];

2. Employing passive or active vibration absorbing devices either at the rotating system or the fixed system [7];

3. Direct modification of the excitation forces, principally aerodynamic forces to reduce vibration.

The first and second categories involve installation of vibration absorbing devices which produce counteracting inertial and damping forces. They are still used in most of the rotorcraft flying today although they also bring unavoidable penalties in terms of weight and tend to affect vibrations only at discrete points. Therefore, an effort to modify directly the excitation forces has been sought by the helicopter community, that is, to eliminate or reduce vibrations by modifying unsteady aerodynamic forces acting on the rotor blades. During the last two decades, this has been investigated and different implementations were attempted. Higher harmonic control (HHC) and individual blade control (IBC) are the typical examples of these efforts. Higher harmonic control is accomplished by manipulating a conventional swashplate to enable blade pitch control of a higher multiple frequency than an integer multiple of rotating frequency, i.e., $(kb \pm 1)$/rev. Individual blade control installs a feathering actuator in each blade rather than modulating the swashplate, and allows for blade pitch control at arbitrary frequencies. Several outstanding results were obtained regarding vibration reduction capability of these concepts, and they comprise of analytical studies searching for an optimal control scheme [8, 9, 10], wind tunnel tests with either small

1.3 Previous Work Related with Integral Twist Actuation

1.3.1 Actuators Applicable for the Integral Concept

An anisotropic actuator is required for the implementation of integral blade twist actuation with certain required characteristics. First, it must be flexible enough to be inserted in the curved shape of the blade assembly. Also, it should have its own structural integrity to withstand the pressure applied during blade fabrication and the external loads during the blade operation. It must have high levels of strain-inducing capability at an appropriately applied electric field. Anisotropy of the actuation is required so that tailoring in the blade design may be possible. Finally, cheap actuator is preferred considering the final blade cost. Candidates which are presently available include Active Fiber Composites (AFC) and Macro-Fiber Composites (MFC).

The AFC is an anisotropic, conformable actuator, which can be integrated with the passive structure [34]. It was originally developed at MIT and now being commercialized by Continuum Control Corporation, Billerica, Massachusetts. The AFC actuator utilizes interdigitated electrode poling and piezoelectric fibers embedded in an epoxy matrix. This combination results in a high performance piezoelectric actuator laminate with strength and conformability characteristics much greater than that of a conventional monolithic piezoceramic. Fig. 1-2 shows AFC packs being inserted in the blade assembly conducted as part of this thesis. However, some disadvantages are also identified for this actuator: difficulty of processing and handling expensive piezoelectric fibers during actuator manufacturing and high actuator voltage requirements. Basic material characterization and proof of concept of an integral twist-actuated rotor blade was investigated at MIT's Active Materials and Structures Laboratory [35].

The MFC has been recently developed at NASA Langley based on the same idea as the AFC in using the piezoelectric fibers under interdigitated electrodes [36]. In this actuator, shown in Fig. 1-3, the piezoelectric fibers are manufactured by dicing from

[30], built and tested a 6-ft diameter two-bladed Froude-scaled rotor model with banks of piezoceramic crystal elements in ±45° embedded in the upper and lower surfaces of the test blade [31, 37]. Using dual-layer actuators, the active blade achieved 0.5° of maximum experimental tip twist actuation, still lower than the 1° to 2° necessary for the possible vibration control applications. Bernhard and Chopra studied another twist concept that incorporates an active bending-torsion actuator beam within the blade spar [28]. Tip twist angles of 0.15° to 0.5° (at 100 V) were achieved during Froude-scaled blade hover test.

The most relevant work for this thesis, however, is the one conducted by Rodgers and Hagood [32] as part of a Boeing/MIT program sponsored by DARPA [38]. They manufactured and hover tested a 1/6th Mach-scaled CH-47D blade in a two-bladed rotor where the integral twist actuation was obtained through the use of AFC. In order to design the blade structure and predict the actuation performance, a rudimentary single-cell active composite beam model [39] was used. Also, an intentional reduction by 50% on the baseline torsional stiffness was imposed and regarded to improve twist actuation. Hover testing on the MIT Hover Test Stand Facility demonstrated tip twist performance between 1° and 1.5° in the rotating environment. Boeing/MIT continues this work that eventually should lead to forward flight wind-tunnel tests and full-scale blade section manufacturing [38].

1.3.3 ATR Blade – Previous Work

Another example of an integral blade twist concept has been studied by the author and his co-workers [33, 40] as part of a NASA/Army/MIT Active Twist Rotor cooperative agreement program. The structural design of the ATR prototype blade employing embedded AFC actuators was conducted based on a newly developed analysis for active composite blade with integral anisotropic piezoelectric actuators [41]. The formulation is one of the first attempts for asymptotically-correct analysis of active multiple-cell beams presented in the literature. The approach is based on a two-step solution of the original three-dimensional electromechanical blade representation by means of an asymptotical approximation: a linear two-dimensional cross-sectional

twist actuation was experimentally observed of 1.1° peak-to-peak.

Even though the new vibration reduction approach using the active materials technology showed promising results from the conceptual point of view [47, 40] and successful preliminary hover testing with small-scaled models [32, 48], experimental forward flight tests were not performed until recently [49]. Moreover, an active aeroelastic environment to design, analyze, and simulate the behavior of integrally-twisted active rotor systems needed to be created. This should impact the ability to design active rotors and will support the design of their control law.

1.4 Present Work

This thesis concentrates on the study of vibration reduction using integral twist actuation on helicopter rotor blades. It includes the development of an analytical framework to identify dynamic characteristics of active rotor system in different flight conditions. The analytical model for forward flight combines a geometrically-exact theory for the dynamics of moving beams with active materials constitutive relations and a finite-state dynamic inflow theory for helicopter forward flight aerodynamics. The solution of this is conducted in time domain. Numerical results from the analytical models are correlated with experimental data obtained from bench, hover and forward flight testing. For this purpose, two main steps are taken. First, a hover testing using the ATR prototype blade previously manufactured is conducted, and the numerical results from the analytical hover model are correlated with the experimental data. Among other things, this step ensures the adequacy of the blade design and evaluates the twist actuation performance in the rotating condition. At the same time, the validity of the proposed analytical framework is demonstrated in both non-rotating and rotating conditions. Secondly, a four-active-bladed rotor system based on the prototype blade design is manufactured and tested in the open-loop control manner for the forward flight condition in the wind-tunnel. In parallel, an active aeroelastic analysis model is upgraded to deal with active twist rotor system during forward flight. Regarding the experimental work, an approach similar to the

helicopter blades

2. Extend it to an aeroelastic analysis framework to simulate helicopter flight with active twist rotor blades and evaluate its response functions

3. Correlate the analytical model with experiments conducted in the bench, hover and forward flight

4. Assess helicopter vibration reduction capability using active twist rotor blades with an appropriate closed-loop control algorithm.

Chapter 2

Analytical Framework

2.1 Introduction

For analyzing helicopter blades with embedded strain actuators, a framework is needed such that the effects of the active material embedded in the structure are kept throughout all the stages of the analysis. The framework should also contain an appropriate aeroelastic analysis component to predict the blade behavior under actuation during different operating conditions such as non-rotating, hover, and forward flight. For this purpose, a specific analytical framework for an active helicopter rotor system is proposed and its schematic is illustrated in Fig. 2-1.

A base element from which the framework originates is the structural model of a general composite beam with embedded anisotropic actuators, and this corresponds to the dashed block at the upper part in Fig. 2-1, designated as "3-D electroelastic beam." In this structural model, an asymptotical analysis takes the three-dimensional electromechanical problem of a rotor blade and reduces it into a set of two analyses: a linear analysis over the cross section and a nonlinear analysis of the resulting beam reference line. Such separation of the blade problem makes it convenient for aeroelastic analysis and consistently accounts for the active material effects. Using the structural model previously developed in [41, 45], the ATR prototype blade design was conducted, and its static twist actuation performance was evaluated [45]. Important elements included in the structural model are recapitulated in this chapter.

The previous structural model is extended and improved in this thesis to investigate the dynamic characteristics of the active rotor system in the bench, hover, and forward flight conditions. This corresponds to the lower dashed block in Fig. 2-1, called "Aeroelastic solution." In this extension, the global beam analysis element from the previous structural model is combined with an appropriate aerodynamics model to compose an aeroelastic system. However, the system is still dependent upon the cross-sectional analysis regarding the beam cross-sectional properties. Solution of the resultant aeroelastic system is obtained in either frequency or time domain, and it includes the blade loads, hub vibratory loads, and blade motion.

Specifically, for hover calculation, a mixed form of the geometrically-exact beam analysis model [44] is modified to account for integral actuation, and combined with finite-state dynamic inflow unsteady aerodynamics [50]. Based on the idea of small perturbation from a steady-state equilibrium position, frequency response functions of the active blade are determined using Laplace transform of the state-space representation. By performing hover analysis, more insight into the fidelity of the present modeling can be explored. Also, the behavior of the integral actuator under rotating condition can be assessed before examining the overall actuation authority of the ATR system.

In forward flight analysis, the same geometrically-exact beam formulation is utilized but in displacement-based form. Also, the forward flight version of the same aerodynamics model is used, and their solution is performed in time domain. For implementation, an existing multi-body dynamics code [51] is modified for the needed active beam analysis. Time domain integration is selected since it is adequate for simulation of the blade response under open-loop actuation. This enables system identification for the sake of modern control, and ultimately closed-loop performance of ATR systems can be studied.

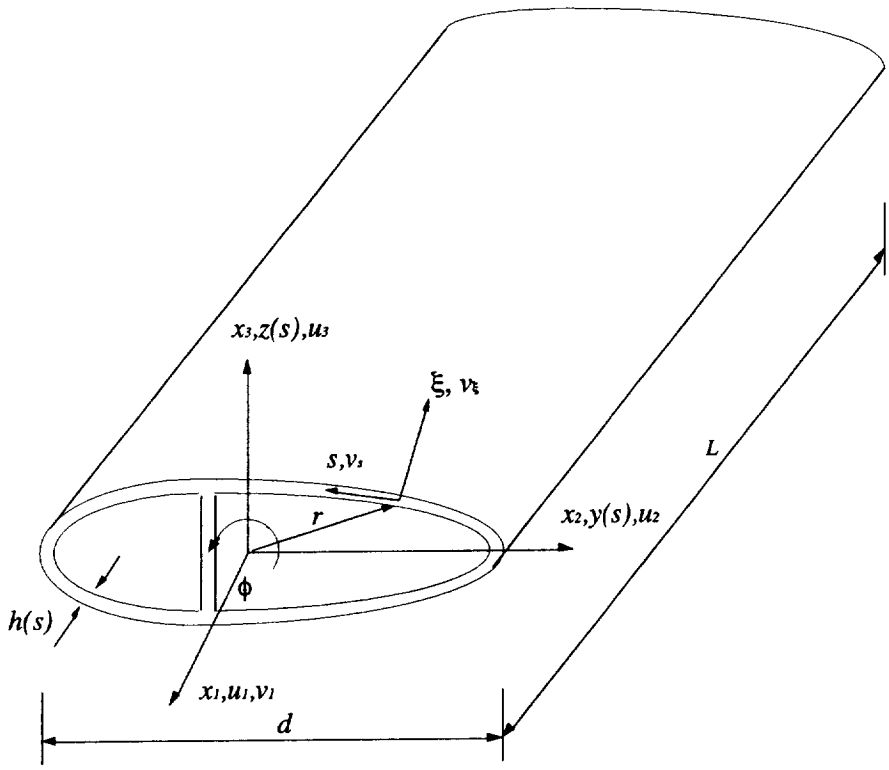

Figure 2-2: Two-cell thin-walled cross section beam

Associated with this displacement field, the beam constitutive relation which relates beam generalized forces (axial force, twist, and two bending moments, respectively) with beam generalized strains (axial strain, twist curvature, and two bending curvatures) and corresponding generalized actuation forces is obtained in the following form:

$$\begin{Bmatrix} F_1 \\ M_1 \\ M_2 \\ M_3 \end{Bmatrix} = \begin{bmatrix} K_{11} & K_{12} & K_{13} & K_{14} \\ K_{12} & K_{22} & K_{23} & K_{24} \\ K_{13} & K_{23} & K_{33} & K_{34} \\ K_{14} & K_{24} & K_{34} & K_{44} \end{bmatrix} \cdot \begin{Bmatrix} \gamma_1 \\ \kappa_1 \\ \kappa_2 \\ \kappa_3 \end{Bmatrix} - \begin{Bmatrix} F_1^{(a)} \\ M_1^{(a)} \\ M_2^{(a)} \\ M_3^{(a)} \end{Bmatrix} \tag{2.2}$$

where $[K_{ij}]$ is the stiffness matrix function of geometry and material distribution at the rotor cross section. γ_1 is the axial strain, κ_1 is the elastic twist, and κ_2, κ_3 are two bending curvatures. The actuation vector is a function of the geometry, material distribution, and applied electric field. Detailed expressions for the stiffness matrix

dependence is assumed linear here, with a linearization of the actuators properties conducted around the operating condition. In practice, some nonlinear behaviors of the ATR prototype blade with respect to applied voltage were observed during bench test [33].

2.3 Global Beam Analysis

2.3.1 Mixed Form for Hover Analysis

The nonlinear one-dimensional global analysis considering small strains and finite rotations is presented here as a direct expansion of the mixed variational intrinsic formulation of moving beams originally presented by Hodges [44], and implemented by Shang and Hodges [54]. The notation used here is based on matrix notation and is consistent with the original work of Hodges [44]. Some steps of the original work are repeated here to help understanding the modifications required in this extended active formulation.

As shown in Fig. 2-4, a global frame named a is rotating with the rotor, with its axes labeled a_1, a_2 and a_3. The undeformed reference frame of the blade is named b, with its axes labeled b_1, b_2 and b_3, and the deformed reference frame named B, with its axes labeled B_1, B_2 and B_3 (though not shown in Fig. 2-4). Any arbitrary vector V represented by its components in one of the basis may be converted to another basis like

$$V_b = C^{ba} V_a, \quad V_B = C^{Ba} V_a \tag{2.4}$$

where C^{ba} is the transformation matrix from a to b, and C^{Ba} is that from a to B. There are several ways to express these transformation matrices. C^{ba} can be expressed in terms of direction cosines from the initial geometry of the rotor blade, while C^{Ba} contains the unknown rotation variables.

The variational formulation is derived from Hamilton's principle which can be written as

$$\int_{t_1}^{t_2} \int_0^l [\delta(K - U) + \overline{\delta W}] \, dx_1 dt = \overline{\delta \mathsf{A}} \tag{2.5}$$

$$\Omega_B = C^{ba}\left(\frac{\Delta - \frac{\tilde{\theta}}{2}}{1+\frac{\theta^T\theta}{4}}\right)\dot{\theta} + C^{Ba}\omega_a \tag{2.7}$$

where u_a is the displacement vector measured in the a frame, θ is the rotation vector expressed in terms of Rodrigues parameters, e_1 is the unit vector $[1,\ 0,\ 0]^T$, Δ is the 3×3 identity matrix, v_a and w_a are the initial velocity and initial angular velocity of a generic point on the a frame. $\dot{(\ )}$ is a derivative with respect to time, and $(\ )'$ is a derivative with respect to the spanwise curvilinear coordinate. $\tilde{(\ )}$ operator applied to a column vector is defined as $\tilde{(\ )}_{mn} = -e_{nmk}(\ )_k$, with e_{nmk} being the permutation tensor.

To form a mixed formulation, Lagrange's multipliers are used to enforce the satisfaction of the kinematical equations, Eq. (2.7).

Manipulating the equations accordingly [54], one can obtain the a frame version of the variational formulation based on exact intrinsic equations for dynamics of moving beams as

$$\int_{t_1}^{t_2} \delta\Pi_a \, dt = 0 \tag{2.8}$$

where

$$\begin{aligned}
\delta\Pi_a = & \int_0^l \{\delta u_a'^T C^T C^{ab} F_B + \delta u_a^T [(C^T C^{ab} P_B)^{\cdot} + \tilde{\omega}_a C^T C^{ab} P_B] \\
& + \overline{\delta\psi}_a'^T C^T C^{ab} M_B - \overline{\delta\psi}_a^T C^T C^{ab}(\widetilde{e_1+\gamma}) F_B \\
& + \overline{\delta\psi}_a^T [(C^T C^{ab} H_B)^{\cdot} + \tilde{\omega}_a C^T C^{ab} H_B + C^T C^{ab} \widetilde{V}_B P_B] \\
& - \overline{\delta F}_a^T [C^T C^{ab}(e_1+\gamma) - C^{ab} e_1] - \overline{\delta F}_a'^T u_a \\
& - \overline{\delta M}_a^T (\Delta + \frac{\tilde{\theta}}{2} + \frac{\theta\theta^T}{4}) C^{ab}\kappa - \overline{\delta M}_a' \theta \\
& + \overline{\delta P}_a^T (C^T C^{ab} V_B - v_a - \tilde{\omega}_a u_a) - \overline{\delta P}_a^T \dot{u}_a \\
& + \overline{\delta H}_a^T (\Delta - \frac{\tilde{\theta}}{2} + \frac{\theta\theta^T}{2})(C^T C^{ab}\Omega_B - \omega_a) \\
& - \overline{\delta H}_a^T \dot{\theta} - \delta u_a^T f_a - \overline{\delta\psi}_a^T m_a\} dx_1 \\
& - \left|(\delta u_a^T \hat{F}_a + \overline{\delta\psi}_a^T \hat{M}_a - \overline{\delta F}_a^T \hat{u}_a - \overline{\delta M}_a^T \hat{\theta}\right|_0^l
\end{aligned} \tag{2.9}$$

following transformation and interpolation are applied within each element [54]

$$x = x_i + \xi \Delta l_i, \; dx = \Delta l_i \, d\xi, \; (\,)' = \frac{1}{\Delta l_i} \frac{d}{d\xi}(\,) \tag{2.13}$$

$$\begin{aligned}
\delta u_a &= \delta u_i(1-\xi) + \delta u_{i+1}\xi, & u_a &= u_i \\
\overline{\delta\psi}_a &= \overline{\delta\psi}_i(1-\xi) + \overline{\delta\psi}_{i+1}\xi, & \theta &= \theta_i \\
\overline{\delta F}_a &= \overline{\delta F}_i(1-\xi) + \overline{\delta F}_{i+1}\xi, & F_B &= F_i \\
\overline{\delta M}_a &= \overline{\delta M}_i(1-\xi) + \overline{\delta M}_{i+1}\xi, & M_B &= M_i \\
\overline{\delta P}_a &= \overline{\delta P}_i, & P_B &= P_i \\
\overline{\delta H}_a &= \overline{\delta H}_i, & H_B &= H_i
\end{aligned}$$

where u_i, θ_i, F_i, M_i, P_i and H_i are constant vectors at each node i, and all δ quantities are arbitrary. ξ varies from 0 to 1.

With these shape functions, the spatial integration in Eq. (2.12) can be performed explicitly to give

$$\begin{aligned}
\sum_{i=1}^{N} & \{\delta u_i^T f_{u_i} + \overline{\delta\psi}_i^T f_{\psi_i} + \overline{\delta F}_i^T f_{F_i} + \overline{\delta M}_i^T f_{M_i} + \overline{\delta P}_i^T f_{P_i} + \overline{\delta H}_i^T f_{H_i} \\
& + \delta u_{i+1}^T f_{u_{i+1}} + \overline{\delta\psi}_{i+1}^T f_{\psi_{i+1}} + \overline{\delta F}_{i+1}^T f_{F_{i+1}} + \overline{\delta M}_{i+1}^T f_{M_{i+1}}\} \\
= \; & \delta u_{N+1}^T \hat{F}_{N+1} + \overline{\delta\psi}_{N+1}^T \hat{M}_{N+1} - \overline{\delta F}_{N+1}^T \hat{u}_{N+1} - \overline{\delta M}_{N+1}^T \hat{\theta}_{N+1} \\
& - \delta u_1^T \hat{F}_1 - \overline{\delta\psi}_1^T \hat{M}_1 + \overline{\delta F}_1^T \hat{u}_1 - \overline{\delta M}_1^T \hat{\theta}_1
\end{aligned} \tag{2.14}$$

where the f_{u_i}, f_{ψ_i} ,$\cdots$, $f_{M_{i+1}}$ are the element functions explicitly integrated from the formulation.

In each element function, γ and κ should be replaced with an expression that is function of F_B and M_B using the inverse of Eq. (2.11), along with the piezoelectric forcing vector $F_B^{(a)}$ and $M_B^{(a)}$. So do V_B and Ω_B with an expression function of P_B

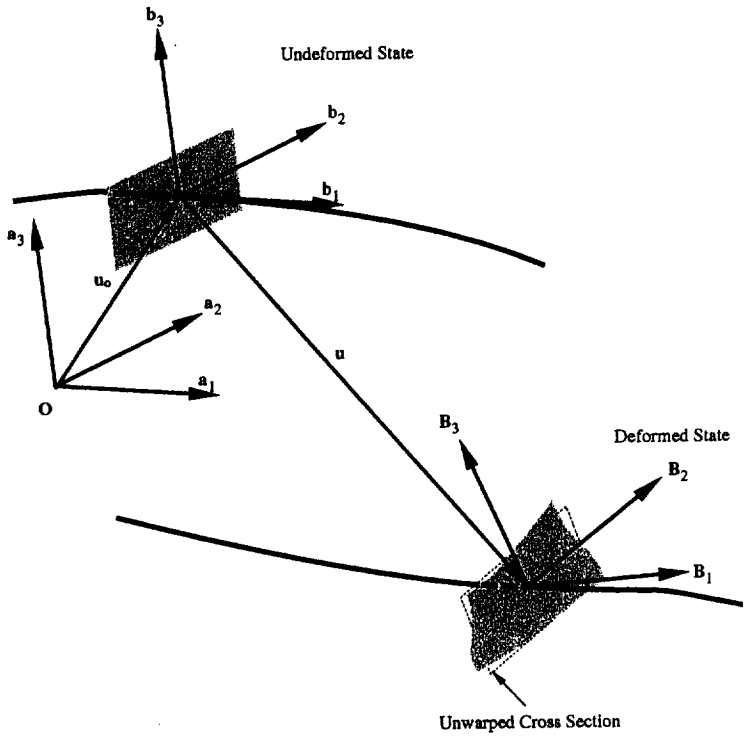

Figure 2-5: Beam in the undeformed and deformed configurations

during forward flight. The integral actuation forces and moments existing inside the blade structure are realized in the form of finite element loads to the passive beam in the modified time domain analysis. In what follows, an overview of the modifications to the formulation for the forward flight analysis is presented.

The kinetic and strain energies of the beam are

$$K = \frac{1}{2}\int_0^L \left\{ \begin{array}{c} V_B \\ \Omega_B \end{array} \right\}^T \left\{ \begin{array}{c} P_B \\ H_B \end{array} \right\} dx_1 \tag{2.17}$$

$$U = \frac{1}{2}\int_0^L \left\{ \begin{array}{c} \gamma_B \\ \kappa_B \end{array} \right\}^T \left\{ \begin{array}{c} F_B \\ M_B \end{array} \right\} dx_1$$

The velocity-displacement and strain-displacement relationships are expressed as

$$\left\{ \begin{array}{c} V_B \\ \Omega_B \end{array} \right\} = \left[\begin{array}{c} C^{ba^T} C^{Bb^T} \dot{\mathbf{u}} \\ C^{ba^T} C^{Bb^T} \boldsymbol{\omega} \end{array} \right] \tag{2.18}$$

Substituting Eqs. (2.19) and (2.11) into (2.21), and integrating by parts yield the governing equations as follows

$$
\begin{aligned}
&(C^{Bb}C^{ba}P_B)^{\bullet} - (C^{Bb}C^{ba}F_B)' = \hat{\mathbf{q}} + (C^{Bb}C^{ba}F_B^{(a)})' \\
&(C^{Bb}C^{ba}H_B)^{\bullet} - \tilde{\mathbf{u}}^T C^{Bb}C^{ba}P_B - (C^{Bb}C^{ba}M_B)' + (\mathbf{u}_o' \widetilde{+ \mathbf{u}'})^T C^{Bb}C^{ba}F_B = \\
&\quad \check{\mathbf{q}} - (C^{Bb}C^{ba}M_B^{(a)})' + (\mathbf{u}_o' \widetilde{+ \mathbf{u}'})^T C^{Bb}C^{ba}F_B^{(a)}
\end{aligned}
\tag{2.22}
$$

where $\mathbf{q}^T = \lfloor \hat{\mathbf{q}}^T,\ \check{\mathbf{q}}^T \rfloor$ are the externally applied loads per unit span, measured in a. As described earlier, the effect of the actuation forcing vector is treated as an additional external load in the right-hand side of Eq. (2.22), while considering the transformation between the inertial frame and the deformed configuration.

2.4 Aerodynamic Analysis

2.4.1 Hover Aerodynamics

The external loads f_a and m_a along the B frame (Eq. 2.9) can be written as:

$$
\begin{aligned}
f_B &= \frac{1}{2}\rho_\infty c a \begin{Bmatrix} 0 \\ (W_{B_3} - \frac{c}{2}\Omega_1)W_{B_3} - \frac{c_{d_o}}{a}W_{B_2}^2 \\ (\frac{c}{2}\Omega_1 - W_{B_3})W_{B_2} - \frac{c}{4}\dot{V}_{B_3} + \frac{c^2}{16}\dot{\Omega}_1 \end{Bmatrix} \\
m_B &= -\frac{1}{32}\rho_\infty c^3 a \begin{Bmatrix} W_{B_2}\Omega_1 - \dot{V}_{B_3} + \frac{3c}{8}\dot{\Omega}_1 \\ 0 \\ 0 \end{Bmatrix}
\end{aligned}
\tag{2.23}
$$

which is based on a thin airfoil theory [57]. Here, ρ_∞ is the air mass density, c is the blade chord length, a is the lift curve slope, c_{d_o} is the profile drag coefficient, W_{B_2} and W_{B_3} are the components of the relative wind velocity in B frame, and Ω_1 is the component of the blade rotational speed along B_1 direction. By the transformation between the frames a and B, these forces and moments are converted to those in

$$\frac{1}{2}\left\{\begin{array}{c}\{\hat{\tau}_n^m\}^c\\ \{\hat{\tau}_n^m\}^s\end{array}\right\} \tag{2.26}$$

where

$$B_{nt}^m = (-1)^{\frac{(n+t-2m-2)}{2}}\sqrt{\frac{H_n^m}{H_t^m}}\sqrt{(2n+1)(2t+1)}\cdot\sum_{q=m,m+2,\ldots}^{n-1} H_q^m\frac{2q+1}{(t-q)(t+q+1)}$$

$[K_n^m]$: diagonal matrix with $K_n^m = \frac{1}{\pi}H_n^m$

$[V_n^m]$: diagonal matrix with

$$V_n^m = \begin{cases}\sqrt{3}\,|a_1^0| & \text{for } (m,n) = (0,1)\\ 2\sqrt{3}\,|a_1^0| & \text{otherwise}\end{cases}$$

where the absolute value is added to ensure the symmetry about the state of zero inflow, or about the zero thrust level. The right-hand side of Eq. (2.26) is regarded as a pressure integral.

2.4.2 Forward Flight Aerodynamics

The same finite-state dynamic inflow aerodynamics model presented in the previous section is also used for forward flight analysis. This aerodynamic theory was originally developed for both hover and forward flight conditions [56]. Moreover, the forward flight part of this model was already implemented in DYMORE.

This model was constructed by applying the acceleration potential theory to the rotor aerodynamics problem with a skewed cylindrical wake. More specifically, the induced flow at the rotor disk was expanded in terms of modal functions. As a result, a three-dimensional, unsteady induced-flow aerodynamics model with finite number of states was derived in time domain. This model falls on an intermediate level of wake representation between the simplest momentum and the most complicated free wake methodologies. It does not require a severe computational effort, which is usually the case in those that involve the vortex filament theory. Therefore, this

can be expressed in the form

$$\begin{Bmatrix} X \\ \\ Y \end{Bmatrix} = \begin{Bmatrix} \bar{X} \\ \\ \bar{Y} \end{Bmatrix} + \begin{Bmatrix} \check{X}(t) \\ \\ \check{Y}(t) \end{Bmatrix} \tag{2.30}$$

where $\bar{(\,)}$ denotes steady-state solution and $\check{(\,)}$ denotes the small perturbation about it.

For the steady-state solution, one has to solve a set of algebraic nonlinear equations originated from Eq. (2.27) and Eq. (2.29):

$$\begin{aligned} &F_S(\bar{X}, 0, \bar{V}) - F_L(\bar{X}, \bar{Y}, 0) = 0 \\ &-F_P(\bar{X}, \bar{Y}) + F_I(\bar{Y}, 0) = 0 \end{aligned} \tag{2.31}$$

The Jacobian matrix of the above set of nonlinear equations can be obtained analytically and, even with the modifications caused by the active material embedded in the structure, it is found to be very sparse. Note that the presence of the actuation in the blade changes the original terms of the Jacobian in a similar manner it does in Eq. (2.14). The steady-state solution can be found very efficiently using Newton-Raphson method.

In order to investigate the dynamic response of the blade with respect to voltage applied to the embedded anisotropic strain actuator, a state-space representation is required once the steady-state solution is obtained. Perturbing Eqs. (2.27) and (2.29) using Eq. (2.30) about the calculated steady state yields

$$\begin{bmatrix} \frac{\partial F_S}{\partial X} - \frac{\partial F_L}{\partial X} & -\frac{\partial F_L}{\partial Y} \\ -\frac{\partial F_P}{\partial X} & \frac{\partial F_I}{\partial Y} - \frac{\partial F_P}{\partial Y} \end{bmatrix}_{\substack{X=\bar{X} \\ Y=\bar{Y}}} \begin{Bmatrix} \check{X} \\ \\ \check{Y} \end{Bmatrix} + \begin{bmatrix} \frac{\partial F_S}{\partial X} - \frac{\partial F_L}{\partial X} & 0 \\ 0 & \frac{\partial F_I}{\partial Y} \end{bmatrix}_{\substack{X=\bar{X} \\ Y=\bar{Y}}} \begin{Bmatrix} \dot{\check{X}} \\ \\ \dot{\check{Y}} \end{Bmatrix} +$$

$$\begin{bmatrix} \frac{\partial F_S}{\partial V} & 0 \\ 0 & 0 \end{bmatrix}_{\substack{X=\bar{X} \\ Y=\bar{Y}}} \{V\} = \begin{Bmatrix} 0 \\ \\ 0 \end{Bmatrix} \tag{2.32}$$

and all other zeros. Eq. (2.35) becomes the second part of a state-space representation with a generalized form as

$$y = \mathbf{C}\check{X} + \mathbf{D}V \tag{2.36}$$

where y is the output vector corresponding to the sensors embedded along the blade.

Frequency response function of the blade can be calculated using Laplace transform of the simultaneous equations which are composed of Eqs. (2.33) and (2.36)

$$\frac{\bar{y}(s)}{\bar{V}(s)} = \mathbf{C}(\mathbf{E}s - \mathbf{A})^{-1}\mathbf{B} + \mathbf{D} \tag{2.37}$$

Note that the coefficient matrix $\mathbf{E}$ is usually singular due to the mixed formulation of the beam model.

2.5.2 Time Domain Solution for Forward Flight Analysis

While the hover analysis presented in the previous section seeks frequency-domain quantities of the blade response function, the forward flight analysis performs a direct time integration of the blade response due to an integral actuation. This is needed since system identification and open- and closed-loop simulations, all in time, must be conducted. DYMORE, the original passive blade dynamics model, adopts a time-discontinuous integration scheme with energy decaying characteristics in order to avoid high frequency numerical oscillation [51, 58]. Such a high frequency oscillation usually occurs during a finite element time integration of a complex multi-body dynamic system. Details of the energy decaying time integration of the beam formulation are found in [51, 58], and briefly summarized in Appendix B.

DYMORE is also capable of adjusting its time step size automatically to maintain stability and accuracy of the integration scheme. Another advantage of adopting multi-body formulation here is that the total shear force and moment exerted by the rotor system can be easily extracted. By adding and monitoring a rigid body element which represents a rotor shaft, the degree of vibratory load variation of the entire rotor system can be directly evaluated. Finally, the control sensitivity functions due to high

Chapter 3

Experimental Setup

3.1 Overview

In the previous chapter, an analytical framework is proposed and established to predict aeroelastic behavior of an active rotor system and numerically evaluate its effectiveness in vibration reduction. At the same time, an experimental effort was pursued to substantiate the present integral blade actuation concept through a small-scale wind-tunnel model. Results from these experiments are also utilized for correlation with the predictions from the proposed analytical framework. Wind-tunnel tests were conducted at NASA Langley's Transonic Dynamics Tunnel as part of the collaboration between the U.S. Army Research Laboratory, at NASA Langley Research Center, and MIT.

The ATR prototype blade was previously designed and successfully manufactured. Preliminary bench testing was conducted to confirm its basic structural characteristics. Details of the relevant work are found in [45], and summarized in this chapter. The prototype blade is used for hover test with three other dummy blades to compose the four-bladed fully-articulated rotor. Blade response under rotating condition is investigated in the hover test. A minor modification is added to the prototype blade design, and four active blades are fabricated based on it. Using four-active-bladed rotor system, forward flight test is performed in an open-loop control manner. The results from the hover, and forward flight tests will be correlated with those predicted

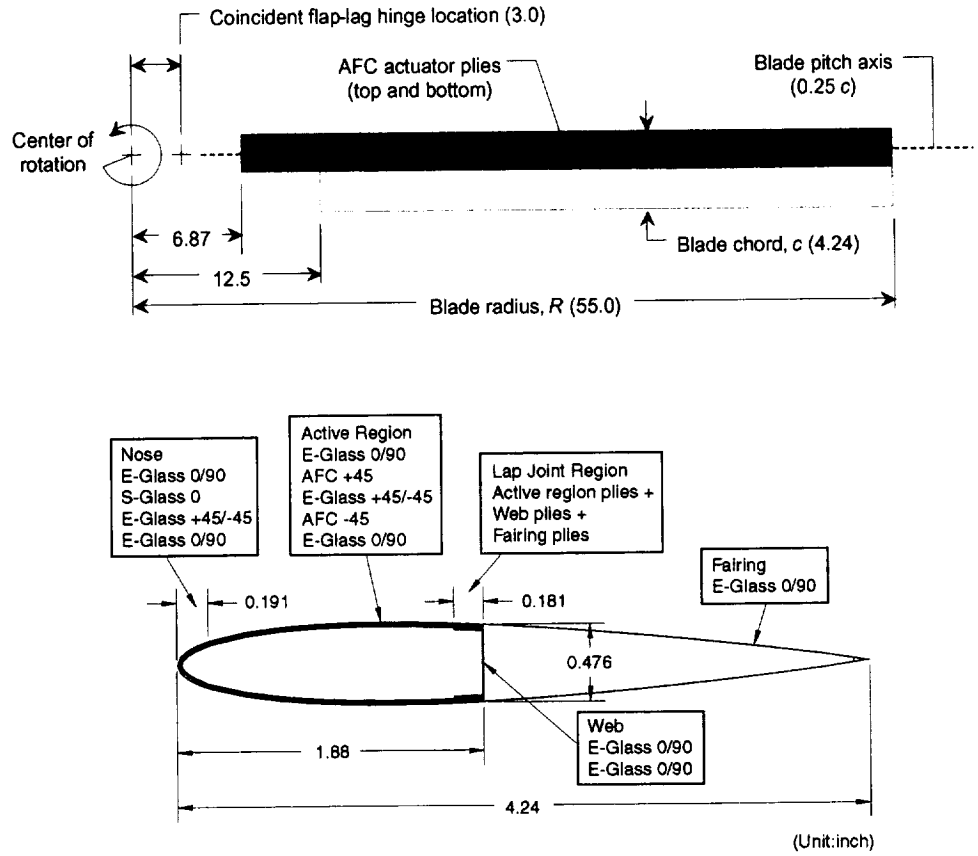

Figure 3-1: Planform and cross-section of the ATR prototype blade (Dimensions are in inches.)

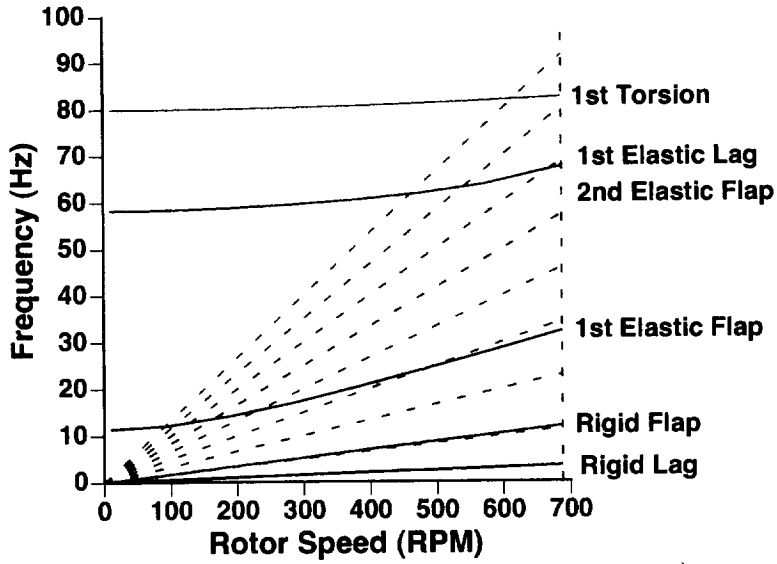

Figure 3-2: Fan plot of the ATR prototype blade from the proposed analysis

prototype blade was originally expected to achieve static twist actuation amplitudes of between 2.0° to 2.5°, and hovering flight dynamic twist actuation amplitudes of 2.0° to 4.0° (based on CAMRAD II and PETRA simulations [40]) at the extended cycle of maximum applied voltage of 4,000 V_{pp}/1,200 V_{DC}. Structural integrity of the new blade design was evaluated based on the worst loading conditions, which are expected to occur within the rotor system operating envelope. In this design, forward flight with the maximum speed is selected as the design loading condition. Then, the largest magnitudes of the aerodynamic loads are extracted and combined with the centrifugal loads in order to give the worst loading values. A safety factor of 1.5 was used.

3.2.2 ATR Test Blade with Modification

Even though experimental structural characteristics and twist performance of the prototype blade compared well with design goals [45], a concern was raised regarding its structural integrity, especially affected by the fatigue loadings. There was not enough experimental evidence that the prototype blade had the fatigue life according to the criterion employed by NASA Langley Research Center for wind-tunnel testing models [59]. Also, an empirical formula adopted by the contractor who planned to build the ATR test blades for forward flight testing indicated that the design should be improved in fatigue [60]. A modification was applied to the design of the prototype blade to compensate this shortcoming. Different lay-up configurations were suggested to increase the structural integrity within the range that its characteristics is not greatly changed from that of the prototype blade. As a result, only one ply of E-Glass fabric prepreg in 0/90° was added to the front spar assembly in order to further withstand centrifugal loading. Using the active cross-sectional analysis previously described, basic structural characteristics were computed for the updated configuration, and listed in Table 3.3. The material properties of the passive prepregs and the AFC plies used in the test blades manufacturing are slightly changed from those in the prototype blade, and are summarized in Appendix D.

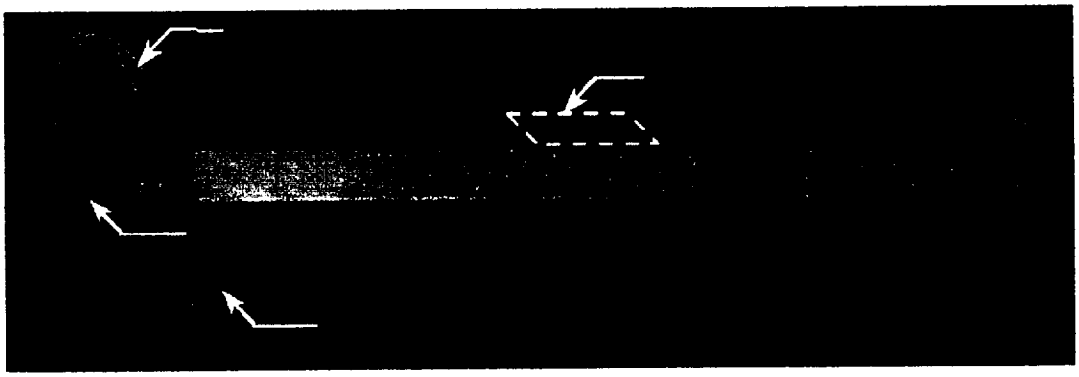

Figure 3-3: ATR prototype blade

3.4 Aeroelastic Tests

3.4.1 Wind Tunnel

The Langley Transonic Dynamics Tunnel (TDT), whose schematic is shown in Fig. 3-4, is a continuous-flow pressure tunnel capable of speeds up to Mach 1.2 at stagnation pressures up to 1 atm. The TDT has a 16-ft square slotted test section that has cropped corners and a cross-sectional area of 248 ft^2. Either air or R-134a, a heavy gas, may be used as a testing medium. The TDT is particularly adequate for rotorcraft aeroelastic testing due to several advantages associated with the heavy gas. At first, the high density of the testing medium allows model rotor components to be heavier, and this satisfies the structural design requirements easily while maintaining dynamic scaling. Second, the low speed of sound in R-134a (approximately 170 m/sec) allows lower rotor rotational speeds to match full-scale hover tip Mach number. Finally, the high-density environment increases Reynolds number throughout the testing envelope, which enables more accurate modeling of the full-scale aerodynamic environment of the rotor system. Both hover and forward-flight tests of the ATR system are primarily conducted in the heavy gas testing medium at a constant density of 2.432 kg/m^3.

3.4.2 Test Apparatus

The Aeroelastic Rotor Experimental System (ARES) helicopter testbed, whose schematic drawing is illustrated in Fig. 3-5, is used for both hover and forward-flight

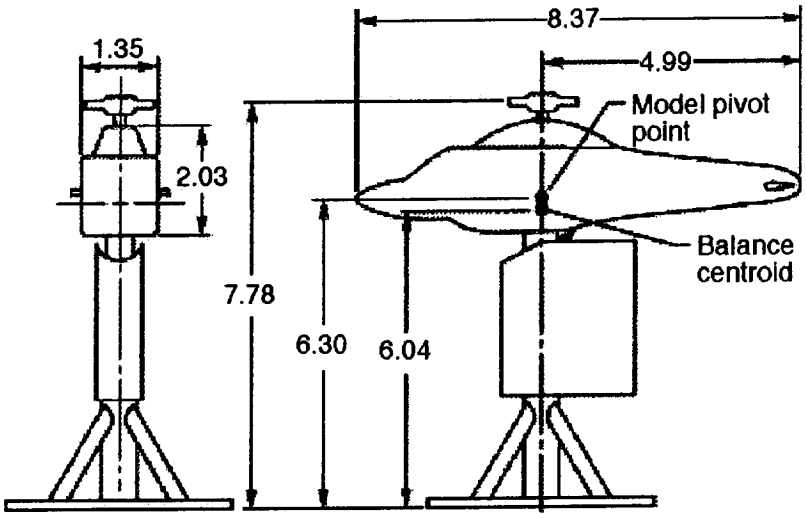

Figure 3-5: Schematic of the Aeroelastic Rotor Experimental System (ARES) helicopter testbed (All dimensions are in ft.) [48]

the fixed-system forces and moments generated by the rotor model. A streamlined fuselage shape encloses the rotor controls and drive system. However, the fuselage is isolated from the rotor system such that fuselage forces and moments do not contribute to the loads measured by the balance.

Fig. 3-6 shows the ATR blades mounted on the ARES helicopter testbed in the TDT. For this configuration a four-bladed articulated hub with coincident flap and lag hinges is used on the ARES. The feathering bearing for the hub is located outboard of the flap and lag hinges, and trailing pitch links are used. The hub is configured such that pitch-flap coupling of 0.5 (flap up, leading-edge down) is obtained and the lag-pitch coupling is minimized. During the hover testing, the test section floor, and the ARES testbed, is lowered approximately 3 ft to allow the rotor wake to vent into the surrounding plenum volume, thus reducing recirculation effects. (In Fig. 3-6, the test section floor is shown in its normal, raised position.).

Table 3.4: Hover test conditions for the ATR prototype blade

Testing medium	Density (kg/m^3)	Rotor speed (rpm)	Collective pitch (deg)	Voltage amplitude (V)
Air	1.225	400	0	100
		400	0	500
		400	0	750
		400	0	1000
Air	1.225	688	0	500
		688	0	1000
		688	4	500
		688	4	1000
		688	8	500
		688	8	1000
		688	12	1000
Heavy gas	2.432	688	0	500
		688	0	1000
		688	4	500
		688	4	1000
		688	8	500
		688	8	1000
Heavy gas	1.546	688	8	1000
	1.984	688	8	1000
	2.432	688	8	1000
	2.432	619	8	1000

to 100 Hz, in 5 Hz increments, at amplitudes of up to 1000 V were applied to the ATR prototype blade. Data from the blade strain gauge bridges, the ARES testbed, and the high-voltage amplifier channels were recorded at a rate of 3,000 samples-per-second by the computer control system for 5-second durations. The signals acquired through the channels during the test are listed in Table 3.5. Even though different loads were measured in the test, correlation with the analytical framework is limited to the blade torsion moments in this thesis. The total rotor loads were measured at the fixed-system balance, and since the dynamics of the fuselage model (housing motors, slip rings for data and power, etc.) is not completely available, these quantities are not included in the present hover analysis model.

The acquired signal data in time were processed to obtain the transmissibility of the system with respect to the sinusoidal actuation of the active blade in frequency

Table 3.6: Forward flight test conditions for the ATR system

	$\mu =$ 0.14	$\mu =$ 0.17	$\mu =$ 0.20	$\mu =$ 0.233	$\mu =$ 0.267	$\mu =$ 0.30	$\mu =$ 0.333	$\mu =$ 0.367
$\alpha_s = +8°$	×							
$\alpha_s = +5°$	×							
$\alpha_s = +4°$	×	×	×	×	×			
$\alpha_s = +2°$	×			×	×			
$\alpha_s = +1°$		×						
$\alpha_s = 0°$	×		×	×	×			
$\alpha_s = -1°$	×	×	×					
$\alpha_s = -2°$	×			×	×			
$\alpha_s = -4°$						×	×	
$\alpha_s = -6°$							×	×
$\alpha_s = -8°$							×	

sine-sweep signal was applied by the high-voltage amplifiers. In case of sine-dwell signals, only 3P, 4P, 5P frequency components were considered since (b+1, b, b-1) frequency components are to influence significantly b-bladed rotor system. Available blade control modes include collective twist, differential twist, and an Individual Blade Control (IBC) mode where each blade actuates according to a prescribed schedule with respect to its position in the azimuthal location. In collective twist mode, all the blades are under the same synchronous twist actuation signals, while those of an opposite sign are transferred to the blade at opposite azimuthal location (e.g., Blade No. 1 and 3) in differential mode. For IBC actuation mode, the actuation on each blade behaves in the same phase at a specific azimuthal location.

Also, a sweeping algorithm over control phase angle was considered within the IBC scheme. It is worth noting that although control phase is indicated by the rotor azimuth (i.e., 0° control phase is coincident with 0° azimuth), control phase is not equivalent to rotor azimuth. For example, a 3P twist actuation with control phase of 180° would impose the maximum twist control at a rotor azimuth of 60°. The second and third cycles would achieve maximum twist control at 180° and 300°, respectively. This will be revisited in the IBC signal generation for the forward flight analysis in Section 5.3.2.

The sine-sweep signal was also used for experimental system identification pur-

Chapter 4

Characteristics of the ATR Blade on the Bench and in Hover

4.1 Overview

Using the ATR prototype blade, two major tests are executed regarding its dynamic response induced by a time-varying electric field applied to the embedded AFC actuators. Bench top non-rotating actuation testing is conducted first. Then, the prototype blade is used to build an active rotor system with the other dummy blades to be tested in hover condition. Details of the hover experiments plan are already introduced in Chapter 3. All these test data are compared with the results from the analytical framework presented before, especially the model which obtains the solution of the aeroelastic system in frequency domain.

4.2 Basic Bench Testing

Different characterization tests were performed on the ATR prototype blade at bench top condition in order to validate the design and manufacturing procedures, and to verify the performance of the prototype article. Also numerical results obtained from the proposed analytical framework were compared with the test data at each stage of the experiments since the model was developed and expanded to enable variety

Table 4.1: Peak-to-peak tip twist actuation of the ATR prototype blade (2,000 V_{pp}/0 V_{DC}, 1 Hz)

	Present Model	Experiment (LDS)	Experiment (PMI)
Spar only	1.4°	1.1°	-
Spar+fairing	1.2°	1.0°	1.1°*

* only 18 active AFC packs.

experimental result from the PMI test is about 15% higher than the original LDS measurements, and the difference from the analytical model is within 12%. This discrepancy was expected and arises from variation in AFC material properties (between packs) and uncertainty in the material properties used in the analysis.

4.3 Non-Rotating Frequency Response

The non-rotating dynamic characteristics of the prototype blade can be evaluated from the frequency response of an applied sinusoidal excitation to the AFC actuators. Figs. 4-1 – 4-4 show the results of the laser displacement sensor (for tip twist angle), the blade strain gauges readings, and the predictions of the frequency domain analysis at several blade stations as function of the AFC actuation.

As one can see, the first torsional mode is clearly identified at approximately 85 Hz, and this result matches well with model prediction. The model neither includes structural nor stationary aerodynamic damping, resulting in infinite peaks at resonance. This already indicates that some structural damping should be added to the model. Once the aerodynamics is included in the problem, its damping will bring that to a finite amplitude. While the strain results could be obtained at high excitation voltages, the dynamic tip twist was measured at low voltages due to the limitation on the range of the laser sensors. At 400 V_{pp}, the peak-to-peak tip twist response of the blade is approximately 3.5°. Such an increased dynamic response around the first torsional natural frequency is expected to affect the twist response over the frequency range of interest when the blade is rotating. It makes the frequency response

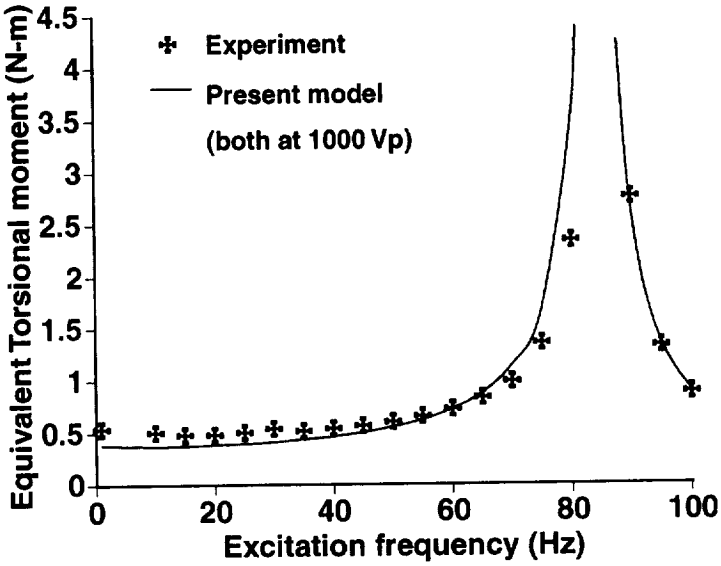

Figure 4-3: Equivalent torsional moment at 49% blade radius of the ATR prototype blade on the bench

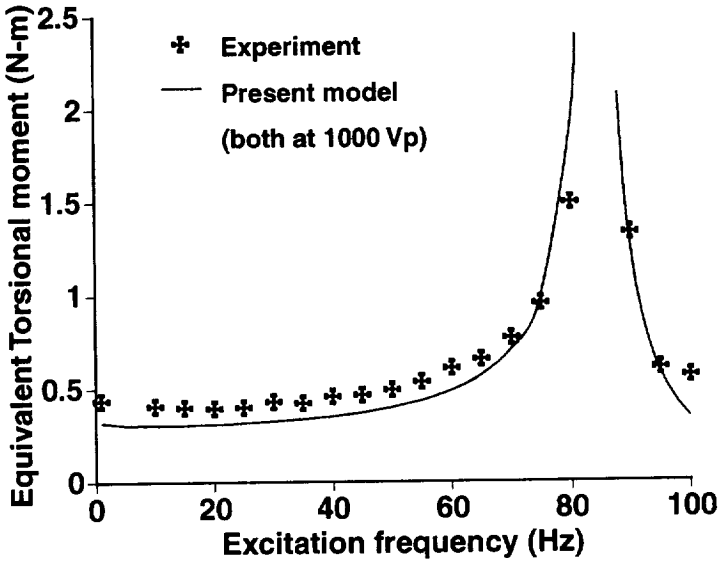

Figure 4-4: Equivalent torsional moment at 75% blade radius of the ATR prototype blade on the bench

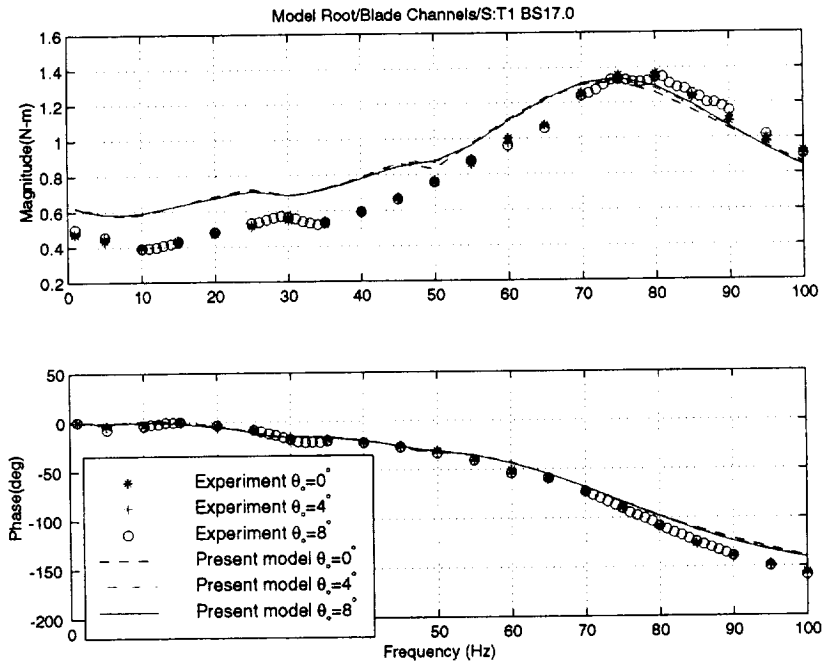

Figure 4-5: Equivalent torsional moment at 31% blade radius of the ATR prototype blade in hover (688 rpm, heavy gas, medium density = 2.432 kg/m^3, 2,000 V_{pp} actuation, θ_o = 0°, 4°, 8°).

varying from 40% to 25%, respectively. This constant offset may indicate the effects of the local three-dimensional deformation field induced by the presence of collocated actuators on the strain gauge bridge, and its effects on strain gauge calibration not taken into account in these results. The phase component of the predicted equivalent torsional moment correlates very well with the experimental results, with errors less than 8% when approaching 10P, which is associated with initial saturation of the power amplifiers during tests.

4.4.2 Medium density sensitivity

When changing the testing medium density, the resulting frequency response functions are shown in Figs. 4-6 and 4-7 for equivalent torsional moment obtained at 31% and 51% spanwise locations, respectively. As one can see, the medium density variation does not influence the actuation authority, except at the torsional resonance frequency due to the change in the aerodynamic damping with density. It is also

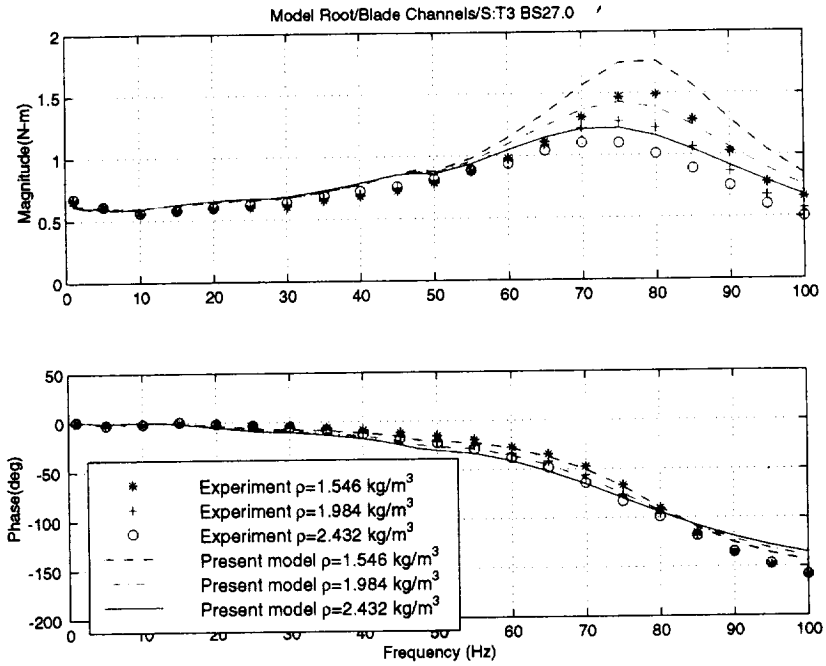

Figure 4-7: Equivalent torsional moment at 51% blade radius of the ATR prototype blade in hover (688 rpm, 2,000 V_{pp} actuation, $\theta_o = 8°$, medium density = 1.546 kg/m^3, 1.984 kg/m^3, 2.432 kg/m^3).

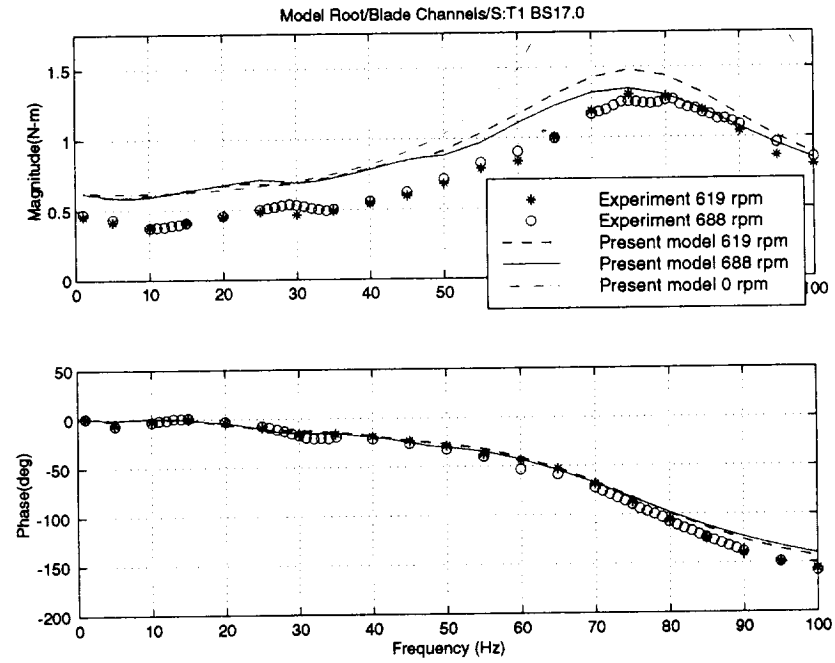

Figure 4-8: Equivalent torsional moment at 31% blade radius of the ATR prototype blade in hover (2,000 V_{pp} actuation, $\theta_o = 8°$, medium density = 2.432 kg/m^3).

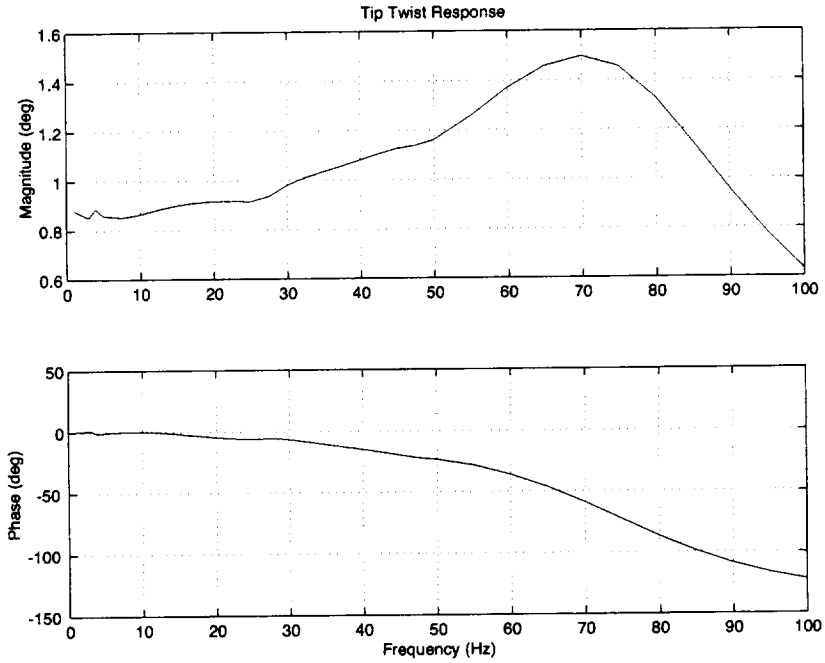

Figure 4-10: Blade tip twist amplitude predicted by the proposed analytical framework (2,000 V_{pp} actuation, 680 rpm, $\theta_o = 8°$, medium density = 2.432 kg/m^3)

the experimental setup to avoid ground and air resonance of the rotor system. The coupled pitch-flap-lag motion may bring some of those effects to influence the results above. Forward flight part of the proposed analytical framework has a capabilty of modeling lead-lag damper, therefore better correlation is expected with regard to this matter.

Since no specific sensor for tip twist measurements were included in the prototype blade, the blade tip twist can only be estimated based on the analytical framework. Fig. 4-10 presents such results. As it can be seen, between 3P and 5P, the blade tip twist amplitude varies between 1.0° and 1.3°, which, according to previous CAMRAD II simulations [40], should be enough to provide 60% to 80% reduction on 4P hub shear vibratory loads. Forward flight test and analysis in Chapter 5 will be addressing this issue in detail.

Chapter 5

Dynamic Characteristics of the ATR System in Forward Flight

5.1 Overview

The forward flight regime is of great interest for the vibration reduction problem. The blade twist control is suggested to alter the undesirable unsteady aerodynamic environment which develops in that flight regime. As mentioned previously, wind-tunnel testing is conducted on the active rotor system with the ATR test blades. At the same time, confidence on the established analysis model for forward flight is to be obtained through its correlation with experimental data.

Initially, the bench top static actuation testing is revisited in this chapter. This is to exemplify basic validation of the active time domain analysis. Then, the potential impact upon the fixed- and rotating-system loads by the integral blade actuation during forward flight is examined. Both experimental and analytical efforts focus on an open-loop control and their correlation. By accomplishing this, the present forward flight model can be taken for further analytical tasks related with system identification and closed-loop controller design, which will be introduced in Chapters 6 and 7.

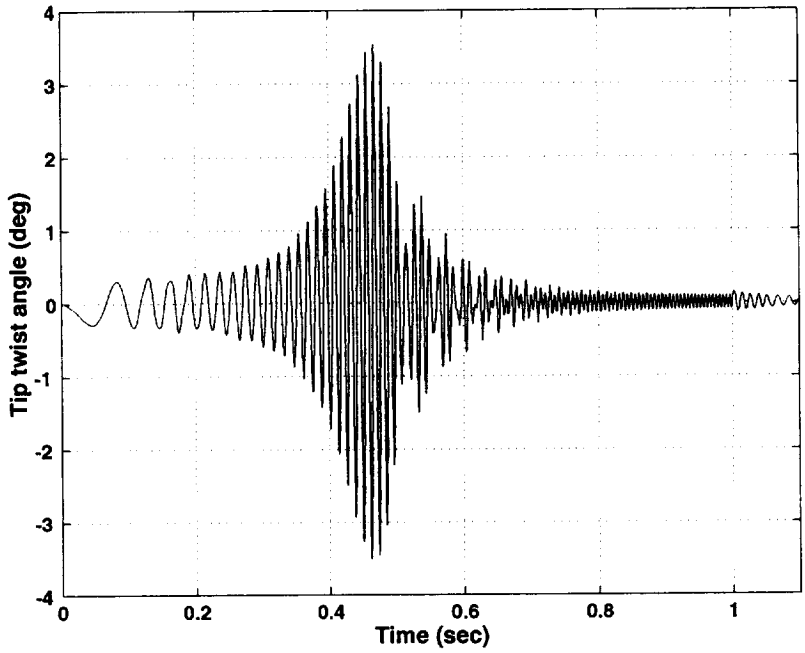

Figure 5-1: Time history of tip twist angle of the ATR blade at bench by sine-sweep actuation signal

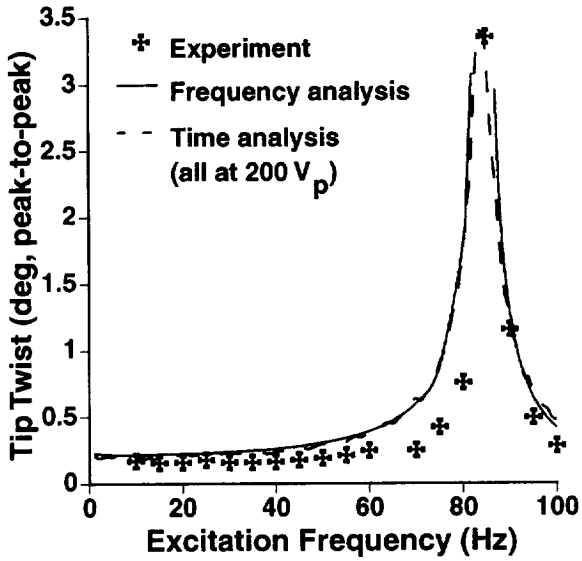

Figure 5-2: Tip twist response of the ATR blade at bench

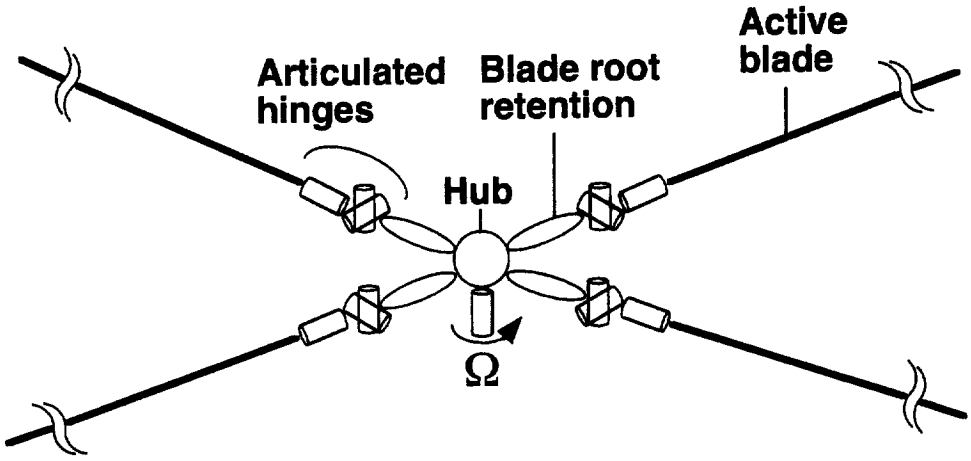

Figure 5-4: Detailed multi-body representation of 4-active-bladed ATR system

to give the hub vibratory loads. Since the ATR system is fully-articulated, three revolute joints are consecutively located between the root retention and the active blade to represent flap, lead-lag, and feathering hinges. As shown in Fig. 5-4, the flapping and lead-lag hinges are coincident. Among the three joints, a prescribed collective and cyclic pitch control commands are applied at the feathering hinge, and their numerical values are based on those used in the wind-tunnel experiment. These are summarized in Table 5.1. Finally, active beams are attached to represent the ATR blades, and they are discretized during the analysis with at least four beam elements per blade, each with the 3rd-order interpolation polynomials. Therefore, there are approximately 900 degrees of freedom to be solved at each time step, including the

Table 5.1: Trim control inputs for the forward flight test conditions

Advance ratio	Rotor shaft inclination angle (deg)	Collective Pitch (deg)	Longitudinal cyclic pitch (deg)	Lateral cyclic pitch (deg)
0.14	-1.0	7.5	-3.5	-3.1
0.17	-1.0	7.0	-3.6	-3.0
0.20	-1.0	7.1	-3.9	-3.1
0.233	-2.0	7.5	-4.3	-3.3
0.267	-2.0	7.8	-4.8	-3.4
0.30	-4.0	8.0	-5.0	-3.3
0.333	-6.0	10.7	-6.2	-4.2
0.367	-6.0	11.2	-6.7	-4.4

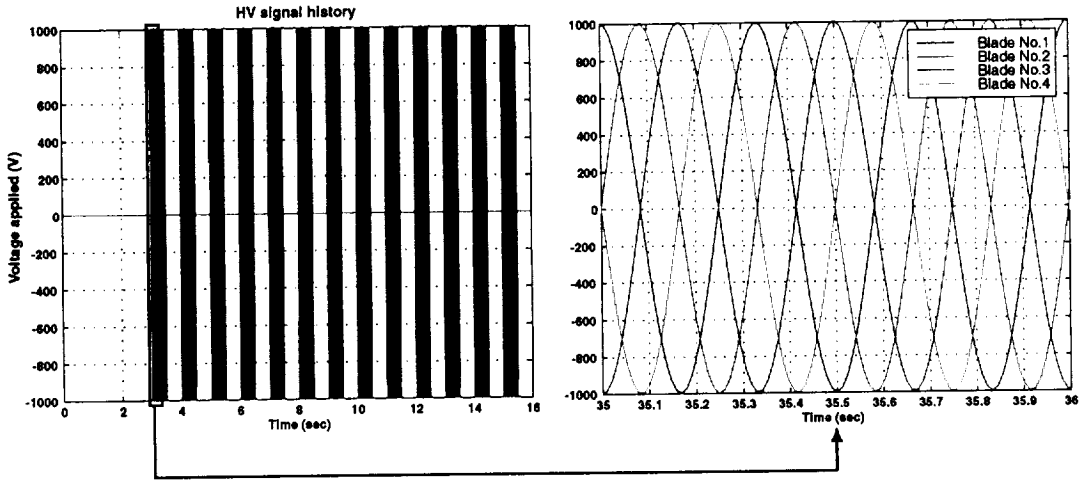

Figure 5-5: Example of high-voltage input generated for an IBC-mode 3P actuation with 12 divisions of control phase angle

those under actuation. Then, for each 0.5-s period of actuation, each with different control phase angle, and another 0.5-s period of no actuation is applied between them. These are applied one after the other as shown in Fig. 5-5.

In each 0.5-second period of actuation cycle, there exists a sine-dwell signal corresponding to a frequency 3P with different phase angles for each blade. 3P sine-dwell signals generated in this fashion are clearly seen in the magnified plot at the right side in Fig. 5-5. By applying this control phase algorithm, the blades exhibit the maximum amplitudes of the sinusoidal electric field at certain azimuthal locations as exemplified in Fig. 5-6. The maximum amplitude occurrence during the first and second actuation periods shows an azimuthal difference of 10° corresponding to 120°/12 divisions, although it is designated as a phase difference of 30° corresponding to 360°/12 divisions in terms of control phase.

5.3.3 Results of the Model without Pitch Link

As a result of the simulation, a time history of the quantities of interest, for example, the forces and moments exerted at each blade and root retention, blade tip displacements, flapping and lead-lag motions at the articulated hinges, and aerodynamic forces generated at the blades are recorded. Among the flight conditions tested

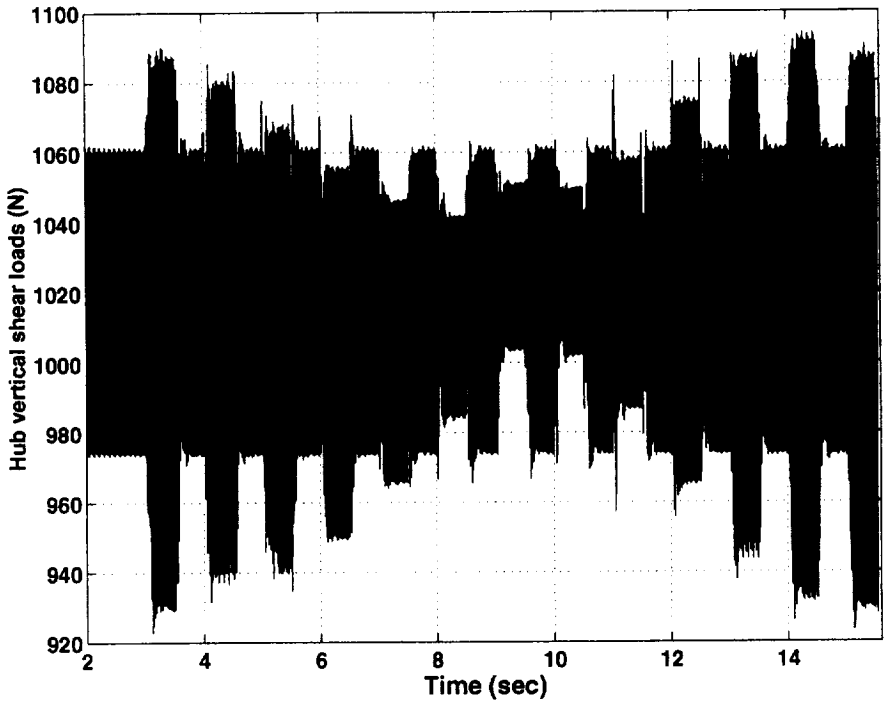

Figure 5-7: Simulated time history of hub vertical shear forces when the 3P actuation is applied as described in Fig. 5-5

for 3P, 4P, 5P actuation applied during the same steady-state trim condition. In the figures, the lines are simple interpolation of the solution points which are obtained from the analysis at discretely increased control phase, while the experimental data are still displayed with the discrete symbols.

The variation of the 4P hub vibratory load components are calculated with respect to the variation of the control phase angles in the vertical, forward, and sideward directions, respectively. The hub sideward component is not included in Fig. 5-8 since its magnitude is too high compared to the other force components, indicating a problem with the measuring device.

The load predicted from the analysis shows significant discrepancy in amplitude from the experimental results, although their variation trends in terms of control phase are in good agreement. As one can see from Fig. 5-8, 3P frequency sine-dwell actuation appears to be the most effective in reducing the hub shear vibratory loads in both cases of vertical and forward components. More specifically, 3P actuation is most effective in hub vertical shear load reduction, resulting in 95% reduction at

210° control phase. It also reduces the hub forward shear loads by 80% at about 180° control phase. Such a hub shear vibratory load reduction performance numerically predicted here shows similar trend as it was observed in the experiment. Further discussion on the comparison between the current analytical results and the experimental data will be given at the end of this chapter. Since the dynamics of the test apparatus (ARES) used for the wind-tunnel test is not included in the model, this may be responsible for the discrepancies. Upgraded input model for the same ATR system including the pitch link and all the linkage components in the swashplate is attempted for better correlation, and will be described in a later section. Also, experimental characterization of the ARES testbed used in the wind-tunnel test is expected to be conducted in the future for the precise modeling of these extra components.

Rotating-system loads in the low-speed level flight case

Quantities in the rotating frame, for example, the flap and chordwise bending moments, and torsional moments are calculated in the reference blade and can also be correlated with the experimental results. The span location where these quantities are calculated is selected to match those of the strain gauges embedded in the test blade. While the fixed-system quantities, such as hub shear vibratory loads, were investigated only in 4P frequency components, those in the rotating frame are extracted and examined in their 3P, 4P, and 5P frequency components. Figs. 5-9 – 5-10 show blade loads at those frequencies.

Again, the lines are simple interpolation of the solution points from the analysis, and symbols represent the experiments. The 3P frequency components of the flap bending moment at 28.7% span location are extracted and shown in Fig. 5-9 (a). The results are for the condition of $\mu = 0.140$, $\alpha_S = -1°$, $C_T = 0.0066$, and 1,000 V twist actuation at 3P, 4P, 5P with respect to control phase. 4P frequency components for the same flap bending moment are presented in Fig. 5-9 (b), and 5P components are in Fig. 5-9 (c). As well as in the fixed-system quantities, the present model captures the trend of variation in the rotating frame values as they were observed in the experiments. However, discrepancies can be observed in the amplitude by approximately

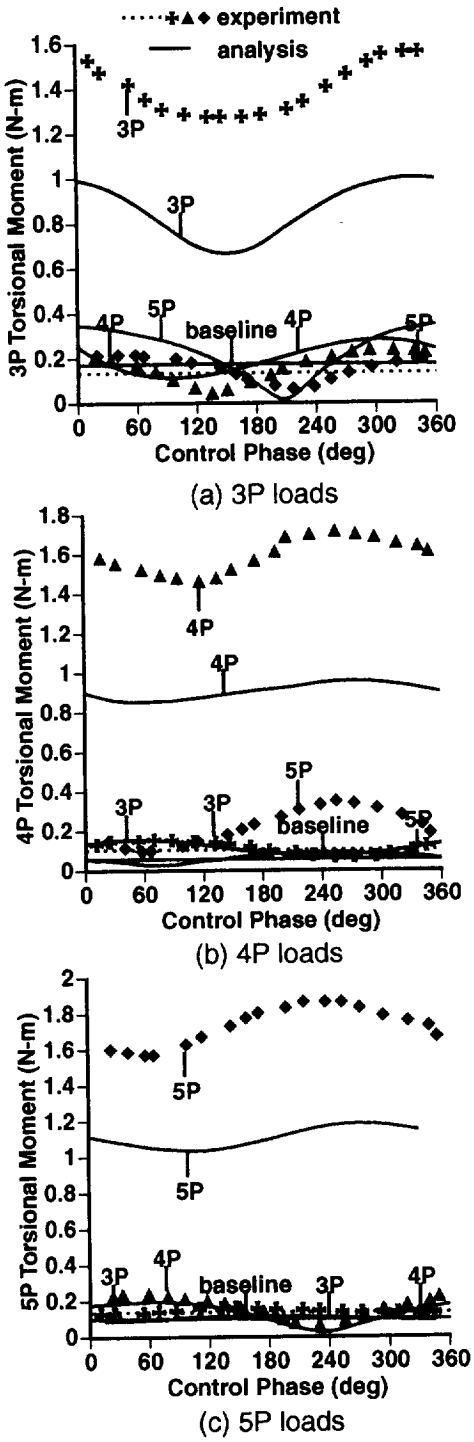

Figure 5-10: Variation of torsional moment at 33.6% span location for $\mu = 0.140$, $\alpha_S = -1°$, $C_T = 0.0066$, and 1,000 V twist actuation at 3P, 4P, 5P with respect to control phase

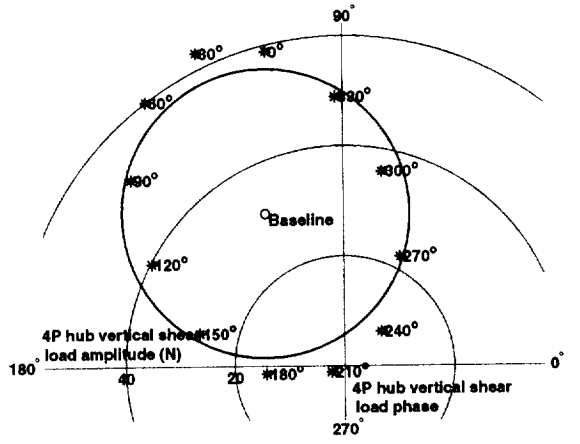

(a) Vertical

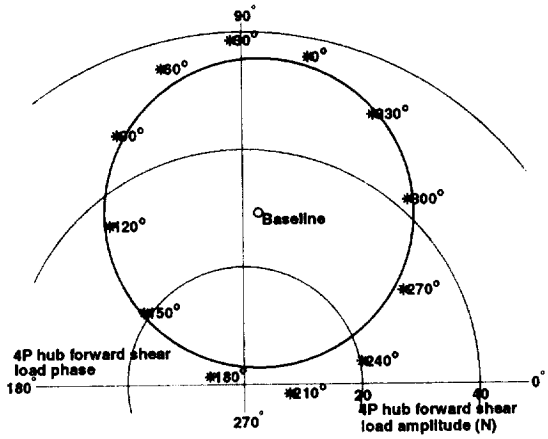

(b) Forward

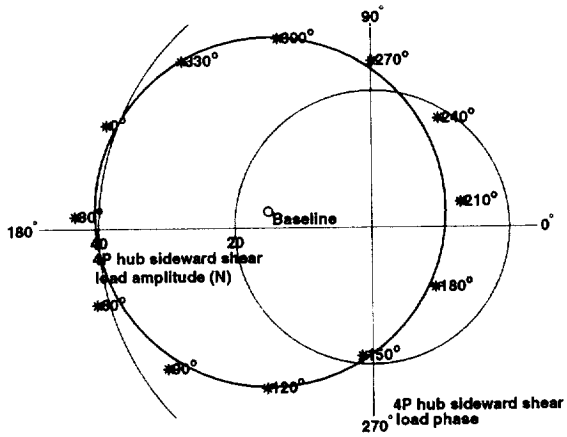

(c) Sideward

Figure 5-11: Polar plot of 4P hub shear vibratory loads for $\mu = 0.140$, $\alpha_S = -1°$, $C_T = 0.0066$, and 1,000 V twist actuation at 3P, compared with the baseline value

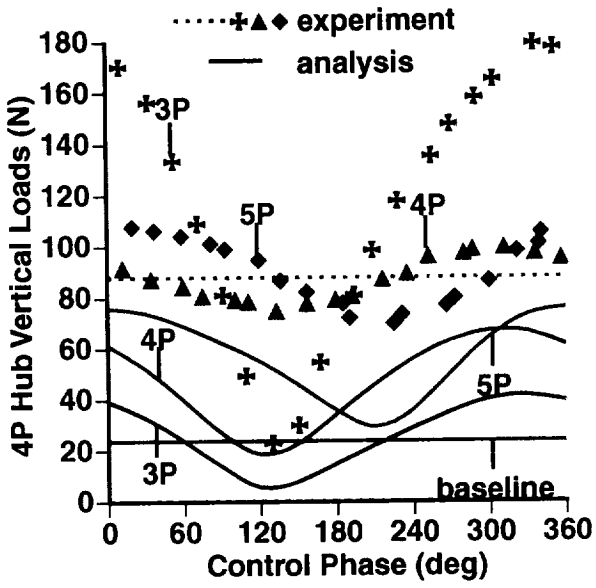

(a) Vertical

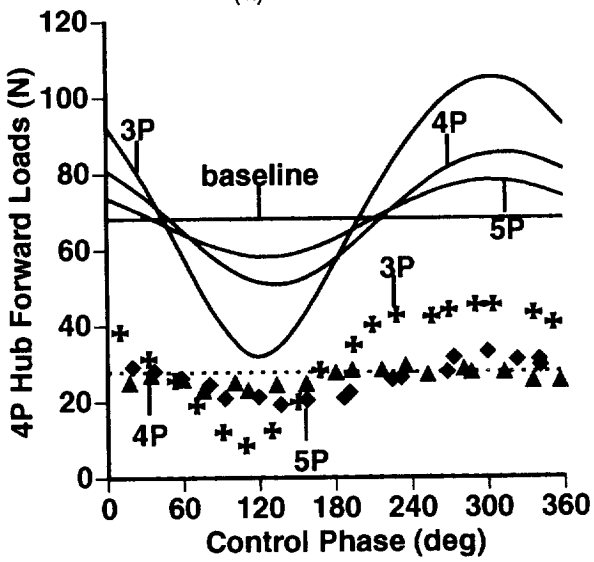

(b) Forward

Figure 5-12: Variation of 4P hub shear vibratory loads for $\mu = 0.333$, $\alpha_S = -6°$, $C_T = 0.0066$, and 1,000 V twist actuation at 3P, 4P, 5P with respect to control phase

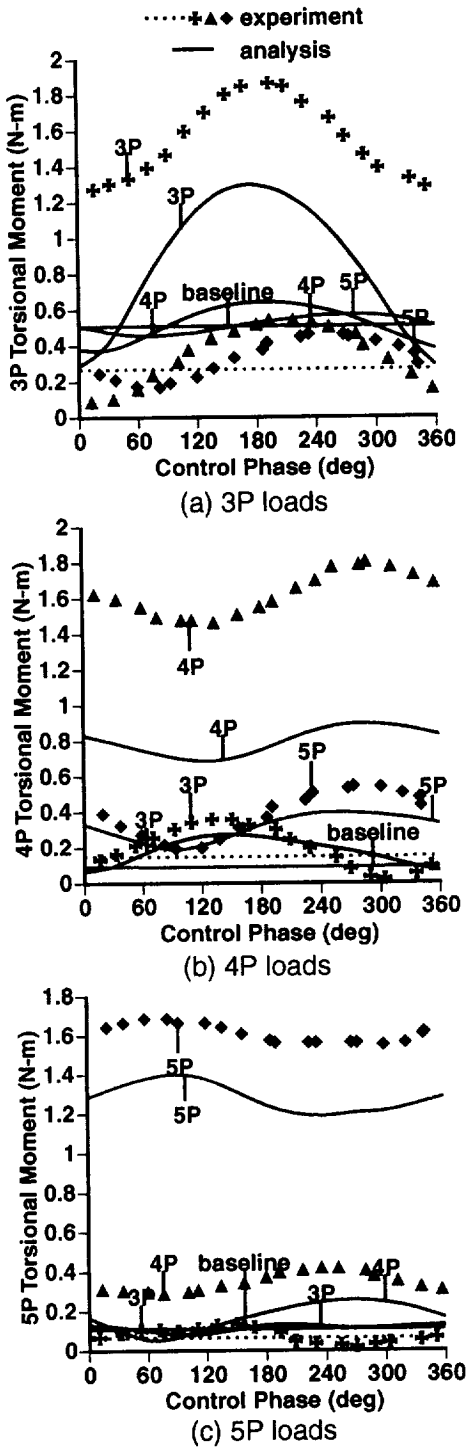

Figure 5-14: Variation of torsional moment at 33.6% span location for $\mu = 0.333$, $\alpha_S = -6°$, $C_T = 0.0066$, and 1,000 V twist actuation at 3P, 4P, 5P with respect to control phase

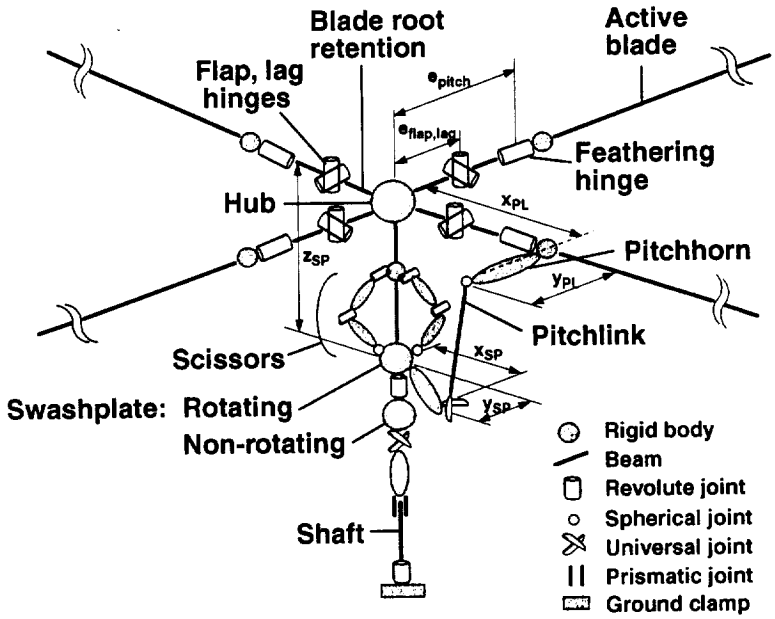

Figure 5-15: Upgraded input model of ATR system including pitch link and swashplate components

flexibility of the whole control system. According to NASA Langley, the rigid feathering mode of the ATR system is observed at frequency between 15P and 16P. Based on the pitch inertia of the ATR test blade and pitch link geometry, an axial stiffness of the pitch link is estimated as also included in Table 5.2. By including the pitch link mechanism in the model, the pitch/flap coupling existing in the ARES apparatus, which amounts to 0.5 in flap up/leading edge down fashion, is automatically implemented. Due to the dynamic interaction among the control linkage, the feathering motion at the blade root in the rotating condition shows discrepancy from those in

Table 5.2: Geometry and material property of the upgraded ATR system model

Parameter	Value
$e_{flap,\ lag}$	0.0762 m
e_{pitch}	0.1143 m
x_{PL}	0.03556 m
y_{PL}	0.05715 m
x_{SP}	0.027686 m
y_{SP}	0.04445 m
$EA_{pitch\ link}$	3.822 10^3 N

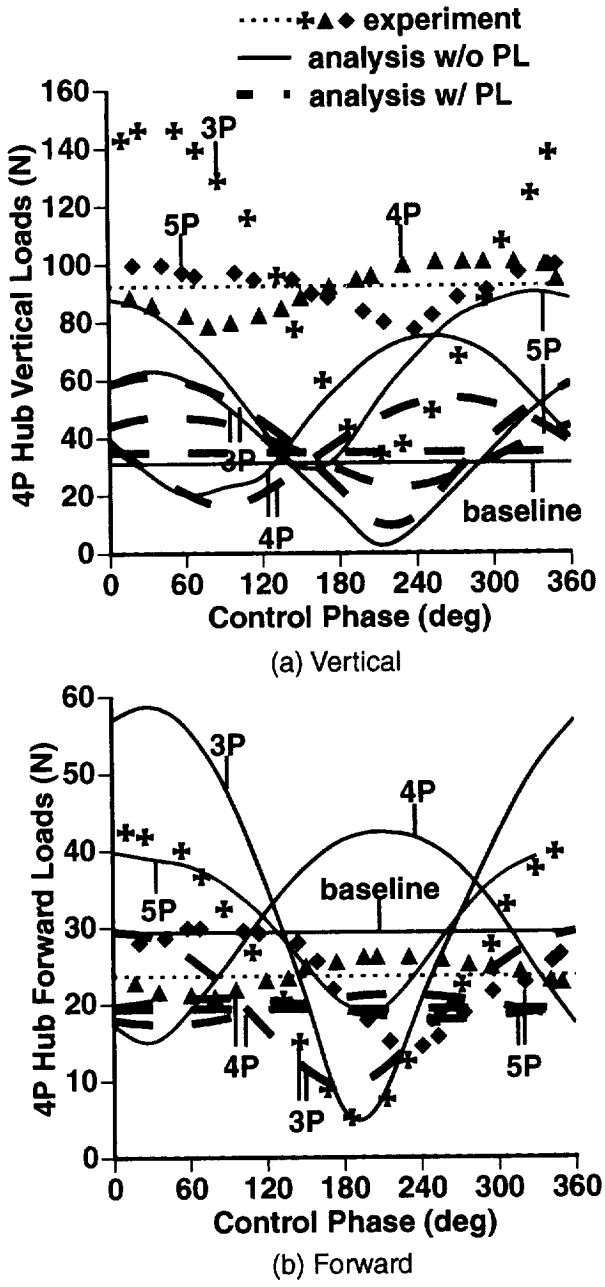

Figure 5-16: Variation of 4P hub shear vibratory loads for $\mu = 0.140$, $\alpha_S = -1°$, $C_T = 0.0066$, and 1,000 V twist actuation at 3P, 4P, 5P with respect to control phase: experiment, analysis without pitch link, and analysis with pitch link

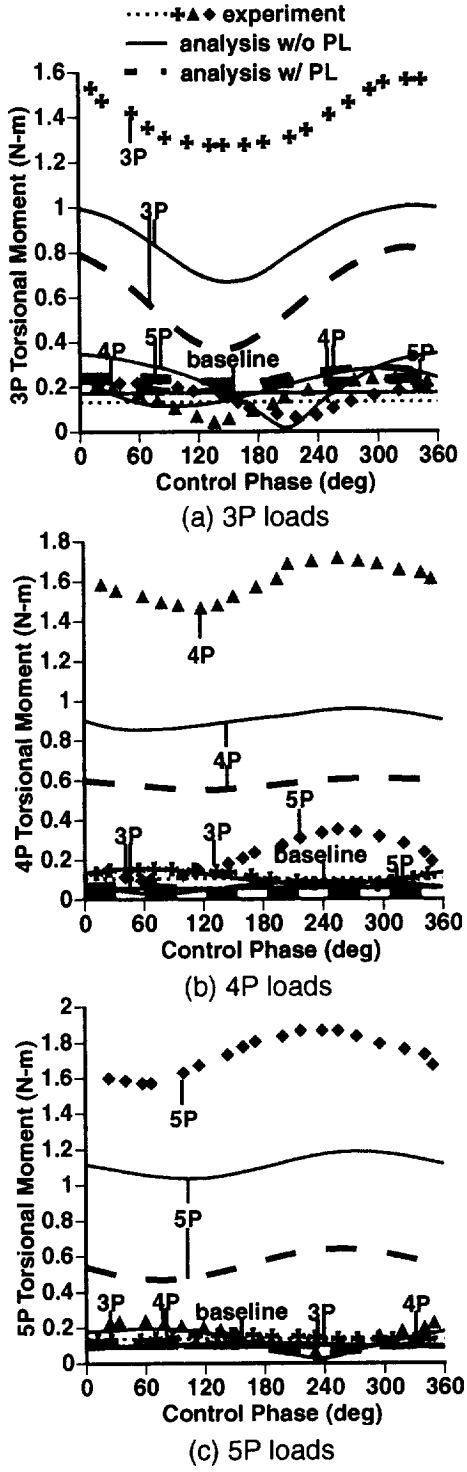

Figure 5-18: Variation of torsional moment at 33.6% span location for $\mu = 0.140$, $\alpha_S = -1°$, $C_T = 0.0066$, and 1,000 V twist actuation at 3P, 4P, 5P with respect to control phase: experiment, analysis without pitch link, and analysis with pitch link

5.4 Correlation of Forward Flight Analyses with Experiments

Both of fixed- and rotating-system loads predicted from the forward flight analysis exhibit significant discrepancy in amplitude from the experimental results, although their variation trend in terms of control phase is in good agreement. It should be further noted that the baseline amplitude in most of the cases are significantly underpredicted by the numerical analysis.

A study to improve the correlation of the baseline load amplitude is performed. For the analysis model without pitch link, blade structural modeling accuracy was studied with respect to the stiffness matrix and chordwise c.g. location, regarded as factors which affect the dynamics of the rotor system. According to the cross-sectional analysis results shown in Table 3.3, the ATR test blade has its chordwise c.g. at 18%, although the blade manufacturers suggested that the blade had required 25% c.g. location. Also, the analysis indicates that the shear center is located at 30% chord instead of the 25% chord that coincides with the blade reference line. This effect can be included in the analysis by simply using the fully-populated stiffness matrix. Therefore, different models of the ATR dynamics were constructed and their prediction of the baseline loads were obtained for the low-speed level flight condition, as shown in Table 5.3. Changes in the load prediction resulted from the variation in the structural modeling. However, these changes fail to significantly improve the correlation with the experiments. Finally, the model with pitch link did exhibit an improvement even with a crude structural modeling for the blade; however, it is again a slight improvement. Therefore, an analysis model with a diagonal stiffness representation, 30% shear center and 25% c.g. locations, has been used for all the analytical results presented in this chapter, and is also used for further analysis in the following chapters.

Also, the experimental 4P hub sideward baseline force (See Table 5.3) presented unreasonably high magnitude when compared to the other two hub force components. This suggests that further characterization of the whole experimental apparatus is

Chapter 6

System Identification of the ATR System in Forward Flight

6.1 Overview

The forward flight analysis model established in this thesis exhibited sufficient details of a typical helicopter and its rotor blade dynamic behavior, although it showed inaccuracy in amplitude of the predicted loads. Therefore, it is selected to be used in this chapter for system identification of the ATR system in forward flight.

During forward flight, the helicopter rotor blade exhibits an aerodynamic environment which varies itself with a period corresponding to the rotor revolution. This situation is illustrated in Fig. 1-1. This signifies that the helicopter rotor system is basically a linear time-periodic (LTP) system during forward flight. Therefore, a methodology considering this periodicity is required for its characterization. In this thesis, a method is adopted which results in multi-component harmonic transfer functions [62]. The theoretical background of the adopted methodology is briefly summarized in Appendix E with its implementation schemes that include additional assumptions imposed on the transfer functions. The sine-sweep input signals created for computation of such harmonic transfer functions are described in detail in this chapter. The results of the system identification is presented for each different mode of blade actuation. Finally, certain characteristics of the present ATR system

equation, Eq. (6.2), will give the phase angle of the chirp ϕ_c as

$$\phi_c(t) = \left(f_0 t + \frac{f_1 - f_0}{2T_c} t^2 \right) 2\pi \tag{6.3}$$

where the phase is in radians. The sine-sweep signal is generated using the unwrapped azimuthal location quantities. The relation between rotor rotational speed Ω (rpm) and the azimuthal location ψ is

$$\psi = \frac{360}{60} \Omega t \tag{6.4}$$

where time t is in seconds. A pseudo-time $\hat{t}$ is introduced based on the previously established relations, and uniformly distributed phase of N chirps over 360° can be produced by considering the number of the chirps that have already been generated, n_c, and shifting the time vector accordingly, so that

$$\hat{t} = \left[\psi - \left\{ -360 + \mathrm{mod}\left(360 \frac{n_c}{N}, 360 \right) \right\} \right] \frac{60}{360\Omega} \tag{6.5}$$

where "mod" is the modulo function that returns the remainder obtained from the division of two arguments. The constructed chirp signal vector $\mathbf{U_c}$ with amplitude A_c for the rotor system can be represented as

$$\mathbf{U_c} = A_c \sin\left[2\pi \phi_c\left(\hat{t} \right) \right] \mathbf{V} \tag{6.6}$$

where $\mathbf{V}$ is a vector of length b, and collective, cyclic, and differential mode of actuation among the blades can be achieved by adjusting the elements of $\mathbf{V}$. In case of four-bladed rotor system, $\mathbf{V}$ for collective mode will be $[\ 1 \quad 1 \quad 1 \quad 1\ ]^T$, while $[\ 1 \quad -1 \quad 1 \quad -1\ ]^T$ for differential mode. A block diagram which generates the sine-sweep input signals described so far is illustrated in Fig. 6-1, and it is a part of the actual Simulink program used to implement chirp actuation during the forward flight testing.

Using the algorithm established, a collective mode chirp input signal is constructed with the amplitude of 1,000 V and nine phase angle divisions over 360° for the present

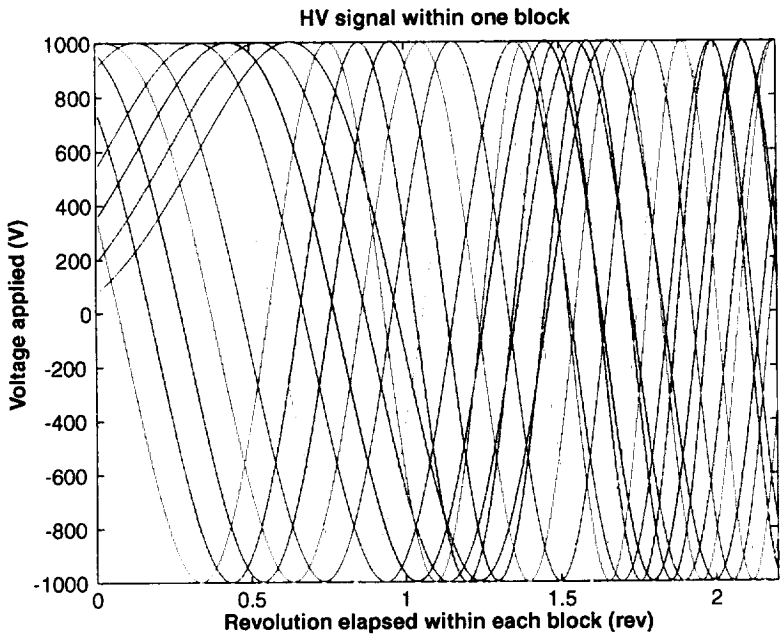

Figure 6-2: Collective mode sine-sweep signals generated with 9 divisions of phase angles

four-bladed ATR system identification. According to the definition of collective mode, all four blades have the same synchronous input signals for actuation, therefore one signal corresponding to Blade No. 1 may become a representative of all the input signals. In Fig. 6-2, representative signal generated for each different phase angle is overlapped with one another along the azimuthal location. It can be clearly seen that the initiation phase angle for each signal is uniformly separated, therefore all the signals conduct one complete sweep of 360° azimuthal location.

6.3 Results of the ATR System Identification

6.3.1 Collective Mode of Actuation

Using the constructed sine-sweep input signal, fixed- and rotating-system response of the ATR system at the low-speed level flight condition which was considered in Chapter 5 are calculated by the time domain analysis. At first, a series of collective mode actuation signal, as shown in Fig. 6-2, is applied, and its response is examined

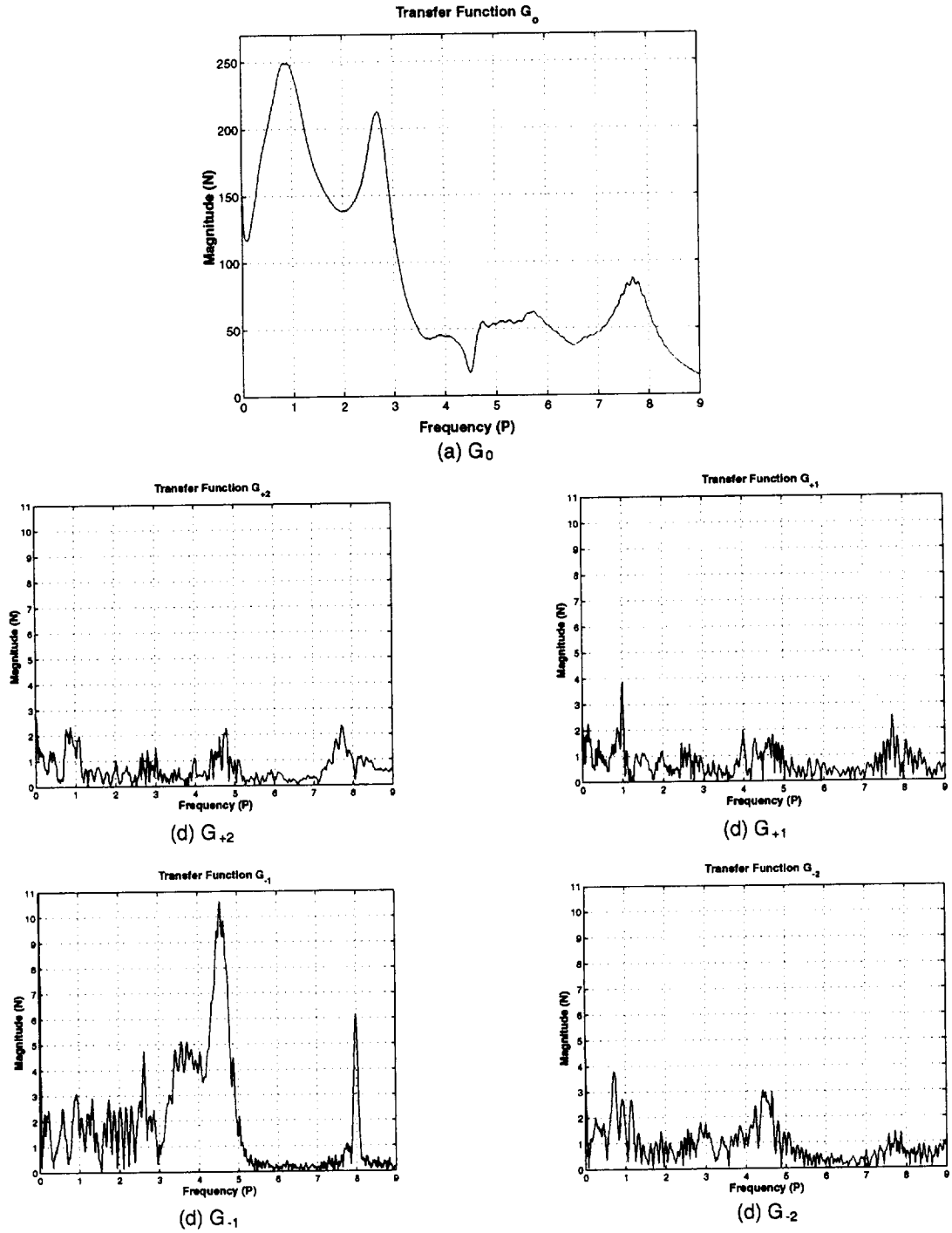

Figure 6-4: Five harmonic transfer functions estimated for the hub vertical shear loads during the collective mode actuation

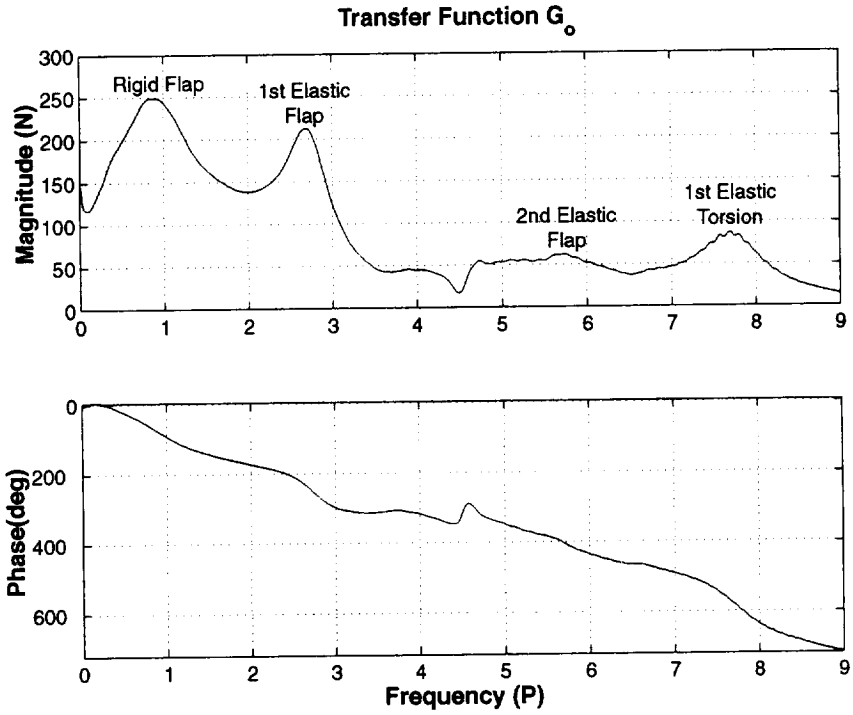

Figure 6-6: Harmonic transfer function G_0 of the hub vertical shear loads during the collective mode actuation

in Fig. 6-6. Furthermore, the property of G_0 being able to approximate the LTP system can be verified by comparing with the polar plot of the hub vertical shear loads obtained in Section 5.3.3. An amplitude of 47 N and phase delay of 317° can be read from the Bode diagram of G_0 in Fig. 6-6 at 4P excitation frequency. This information exactly matches those included in the polar plot of the hub vertical shear loads under the sine-dwell actuation at frequency 4P, which is illustrated in Fig. 6-7. In fact, IBC-mode 4P sine-dwell actuation considered in Chapter 5 generates exactly the same actuation signal as the collective mode considered here. The maximum amplitudes during IBC-mode 4P sine-dwell actuation occur at 90°, 180°, 270° azimuth after blade No. 1, respectively, which eventually places them at Blade No. 2, No. 3, No. 4, respectively. This results in equivalent signal used in the collective mode of actuation. Therefore, both of open-loop control simulation using IBC-mode sine-dwell actuation in Chapter 5 and system identification using sine-sweep actuation here describe the system behavior in a consistent manner.

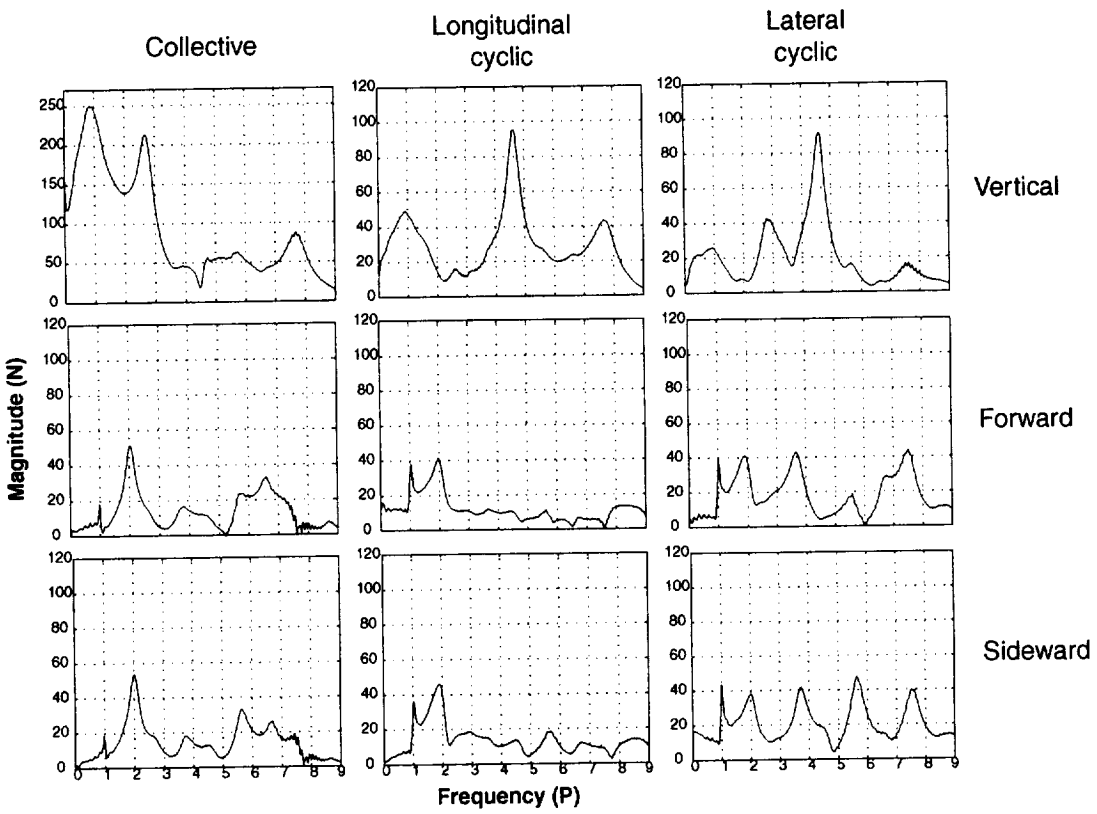

Figure 6-8: Matrix of G_0 estimated for three components of 4P hub shear vibratory loads versus three modes of blade actuation

still valid for these modes of actuation. All the identification results including the collective mode previously obtained may be represented as a transfer matrix relating three components of the hub shear loads versus three modes of blade actuation signal as shown in Fig. 6-8. Note that the vertical component versus the collective mode actuation (the uppermost and leftmost one) is only drawn in different scale from the others for an easy examination of the plots.

This transfer matrix leads to the idea of a multiple-component closed-loop controller which combines the three modes of blade actuation simultaneously. It may be designed for elimination of either single component of hub shear force or multiple-components of them at a time. For example, suppose the case of eliminating only the vertical components of 4P hub shear vibratory loads. From the analytical results presented in Fig. 5-8, the baseline amplitude for this component of the hub vibratory load was predicted as approximately 31 N. However, from Fig. 6-8, the amplitudes

Chapter 7

Closed-loop Controller for Vibration Reduction in Forward Flight

7.1 Overview

The results from system identification in Chapter 6 are utilized here to design a closed-loop controller for hub shear vibratory load reduction. As briefly mentioned in Section 5.3.3., the so-called **T** matrix approach has been traditionally used by researchers investigating higher harmonic control to identify transfer matrix [8, 13]. This approach resulted in a rather complicated structure of a closed-loop controller in order to implement the modulation and demodulation phases of the scheme. However, it was recently found that such a complex controller structure can be reduced to a classical disturbance rejection algorithm [9, 10]. This results in a simple LTI feedback compensator. In this thesis, a closed-loop controller based on this simple structure is attempted. Stability of the closed-loop system is checked first. Then, the vibratory load reduction capability of the designed controller is demonstrated numerically by combining with the time domain analysis built for the ATR system.

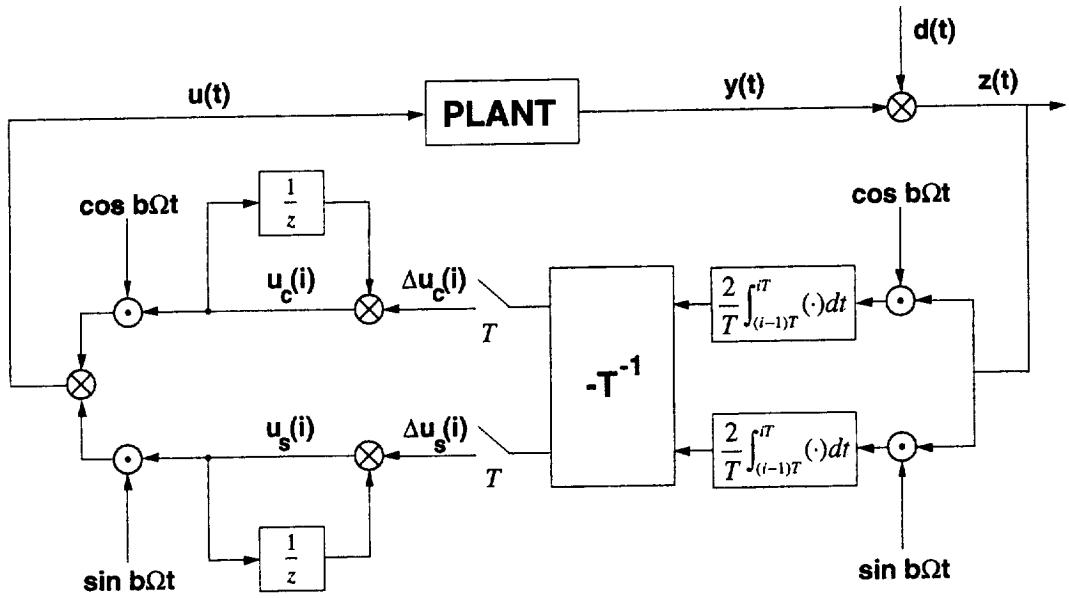

Figure 7-1: Block diagram of the higher harmonic control system adopted by researchers using quasisteady helicopter plant model [9]

output LTI system for a given plant transfer function $G(s)$ [9, 10]. According to this derivation, the block diagram shown in Fig. 7-1 is equivalent to an LTI feedback compensation structure, as illustrated in Fig. 7-2. The feedback compensator, $K(s)$, becomes

$$\begin{aligned} K(s) &= \frac{2k(As + Bb\Omega)}{s^2 + (b\Omega)^2} \qquad (7.3) \\ k &= \frac{1}{T} \\ A = \text{Real}\left\{\frac{1}{G(jb\Omega)}\right\}, &\qquad B = -\text{Imag}\left\{\frac{1}{G(jb\Omega)}\right\} \end{aligned}$$

where T is the blade passage period. Furthermore, this LTI feedback compensator structure turns out to be essentially the same as a classical disturbance rejection algorithm, which is to eliminate an almost pure harmonic signal at constant frequency ω_o with the following compensator

$$H(s) = \frac{c_1 s + c_2}{s^2 + \omega_o^2} \qquad (7.4)$$

Stability and performance issues of the closed-loop system associated with this feed-

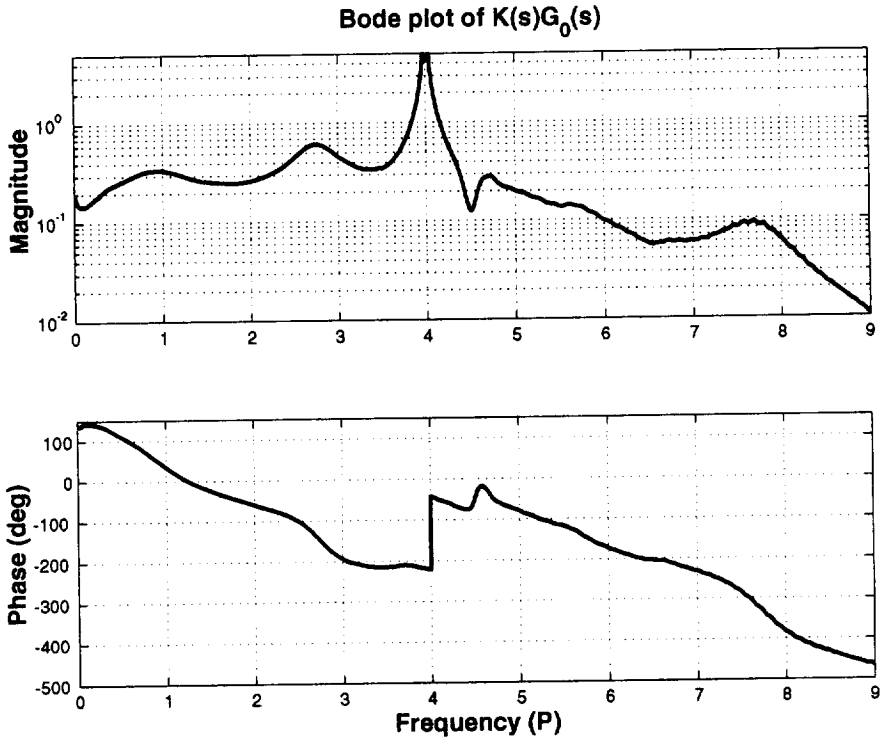

Figure 7-3: Bode plot of the loop transfer function

an infinite weighting at 4P frequency, the gain of the loop transfer function goes to infinity at the same 4P frequency, which makes it exceed unity over a narrow region centered at this frequency. Then, the variation of the phase within this region will determine the stability of the closed-loop system.

Another useful method of checking the stability of the controller is to examine the magnitude versus phase plot (Nichols plot) of the loop transfer function. Nichols plot of the present closed-loop system without any modification applied to $K(s)$ is displayed in Fig. 7-4 (a). The stability of the system is ensured if no encirclements of the critical point (unity magnitude at 180° of phase). This critical point is designated by a small circle in Fig. 7-4. In the same plot, contours of constant disturbance attenuation (or amplification) are also plotted according to the following relation

$$\frac{y}{d} = \frac{1}{1 + K(s)G_0(s)} \tag{7.5}$$

The closed contours around the critical point with positive figures represent degrees of

vibration amplification. The inverted U-shaped contour with thicker line represents 0 dB boundary, where no vibration attenuation or amplification is obtained. The other contours indicate how much attenuation results (in dB) for the corresponding loop gain. Also, along the loop gain line, corresponding frequencies are designated by asterisks to see which frequency content is involved with a possible instability near the critical point. According to Fig. 7-4 (a), the present controller with the original $K(s)$ turns out to have gain margin of approximately 5.4 dB, and phase margin of 36°. In principle, this level of stability margin is regarded as enough for a general feedback compensator.

7.3.2 Modified Feedback Controller

When the gain of the controller is increased, i.e, the closed-loop gain line is shifted upward, there appears a chance of instability since it makes the gain margin diminished. Instability induced from this lack of gain margin is practically manifested during the numerical simulation, which will be described in the following section. Therefore, a modification on the original controller is needed to avoid this type of instability. The solution for this is to alter the closed-loop gain to have new phase characteristics, which is shifted by 45° from its original one. This modification is implemented by changing the transfer function for $K(s)$ in the following way

$$K(s) = \frac{2k(A's + B'b\Omega)}{s^2 + (b\Omega)^2} \tag{7.6}$$

where

$$A' = \text{Real}\left\{(A - jB)e^{j(-45°)}\right\}$$
$$B' = -\text{Imag}\left\{(A - jB)e^{j(-45°)}\right\}$$

where A and B are the same parameters as defined in Eq. (7.3). The resulting controller with the modification generates a new Nichols plot which is shown in Fig. 7-4 (b). Examining the result, the phase of the modified closed-loop gain is shifted as desired. Notice, however, that the magnitude of the closed-loop gain is slightly

all the components of the harmonic transfer functions. In this section, a numerical demonstration of this situation is attempted using the time domain analysis.

The resulting LTI feedback compensator, whose transfer function in continuous-time is described by Eq. (7.7), can be easily incorporated in the time domain analysis by transforming it into a discrete-time state-space approximation. Using the c2d command based on a Tustin approximation, which is provided in MATLAB, an approximately equivalent discrete time state-space representation of the same feedback compensator can be obtained with the specific time step size selected for the analysis. The equivalent LTI feedback compensator which is transformed into the discrete-time state-space version can be expressed as

$$\begin{aligned} \mathbf{x}_{k+1} &= \mathbf{A}\mathbf{x}_k + \mathbf{B}\mathbf{u}_k \\ \mathbf{y}_k &= \mathbf{C}\mathbf{x}_k + \mathbf{D}\mathbf{u}_k \end{aligned} \tag{7.8}$$

where $\mathbf{x}_k$ is the state variables internal to the controller estimated at time step k. $\mathbf{u}_k$ is a sensor measurement from the plant, i.e., hub vertical shear load measurement in this case, and $\mathbf{y}_k$ is a controlled quantity of electric field applied at the blade integral actuators at time k in collective mode. Since the resultant controller is described as a third-order system in Eq. (7.7), its state-space representation involves three state variables, meaning that $\mathbf{x}_k$ becomes a 3×1 vector.

After incorporating the matrix representation described in Eq. (7.8) into the time domain analysis, a simulation is executed in order to evaluate the performance of the closed-loop controller. It is still required to establish the steady-state equilibrium for a specific flight condition before engaging the vibration minimizing controller. Otherwise, huge hub vibratory loads which are induced during the transient period before the steady state equilibrium is reached may generate unrealistically large control signal. Therefore, the initial 3-second period of no actuation is applied again to obtain the trim condition. Then, the controller is engaged with a different magnitude of its gain constant discretely adjusted at 0.5, 1.0, and 2.0 within each 2-second period.

The result of the time domain analysis is displayed as a time history of the hub

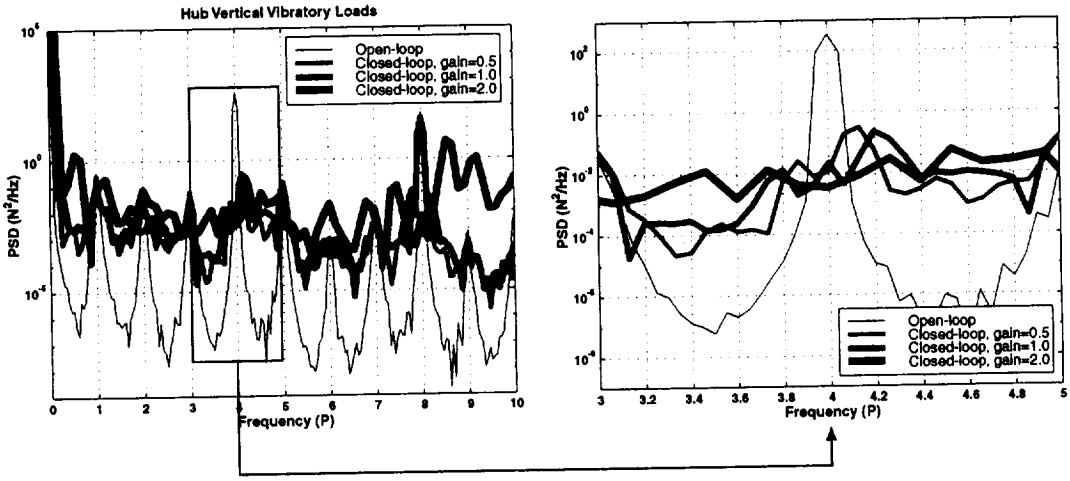

Figure 7-6: Power spectral desnity distribution of the hub vertical shear loads for $\mu = 0.140$, $\alpha_S = -1°$, and $C_T = 0.0066$ without and with the closed-loop controller engaged

that the vibratory component at 4P frequency is decreased by different degree for each gain constant applied. According to this result, more than 90% of the 4P vibratory load existing in the original response is eliminated by the controller engagement. However, outside the narrow band of 4P frequency, it is observed that undesirable increase of vibratory load components are caused by the controller. Also, another significant vibration amplitudes are found at integral multiples of 4P frequency (e.g., amplitude at 8P frequency in Fig. 7-6). These vibration components are rarely affected by the current controller design, and explain the remnant vibration after the 4P component is eliminated. Therefore, it is recommended to improve the present controller into one that can eliminate disturbance in multiple harmonic components [25] in order to reduce other vibration components simultaneously.

Chapter 8

Conclusions and Recommendations

8.1 Summary

This thesis presents the numerical and experimental investigations of integral twist actuation of helicopter rotor blades as a mean to reduce vibration induced in forward flight. Active rotor blade with embedded anisotropic piezoelectric actuators is designed using the analytical framework established in this thesis. An analytical framework is proposed to investigate integrally-twisted helicopter blades and their aeroelastic behavior during different flight conditions. This framework is composed of frequency domain analysis for hover, and time domain analysis for forward flight. Both analyses are based on the same three-dimensional electroelastic beam formulation with geometrical-exactness, and are coupled with the appropriate finite-state dynamic inflow aerodynamics model. A prototype blade is manufactured and bench tests are conducted to confirm its structural characteristics and adequacy of the implementation process. Hover test of a four-bladed fully-articulated rotor is performed using the prototype blade with the other dummy blades. A good correlation is obtained regarding the control sensitivity of the active blade at hover condition. Based on the prototype blade design, four ATR test blades are manufactured in order to compose a fully-active-blade rotor system. This rotor system is tested in the NASA Langley Transonic Dynamics Tunnel in a first-ever forward flight condition for an integrally-twisted rotor.

and on the classical disturbance rejection algorithm. A preliminary stability check was conducted, and the resultant LTI feedback compensator was demonstrated numerically by incorporating it in the time domain analysis model. Even with the original plant with all the LTP components, the designed controller showed a satisfactory vibration reducing capability.

This thesis has addressed several issues related with helicopter vibration reduction technology with integrally-twisted rotor blades, which are:

1. Development of an analysis framework for the rotor system with actively-twisted blades in hover and forward flight
2. Investigation of dynamic characteristics of ATR blade due to its integral actuation at bench and in hover
3. Investigation of impact upon the ATR fixed- and rotating-system loads due to blade twist actuation in forward flight
4. Estimation of harmonic transfer functions of the ATR system in forward flight based on the linear time-periodic system theory
5. Design and numerical demonstration of closed-loop controller which minimizes helicopter vibration by integral blade twist actuation

8.2 Conclusions

A number of conclusions can be drawn from the current helicopter vibration reduction study, and they are summarized as follows.

- Experimental structural characteristics of the prototype blade compare well with design goals, and predictions by the established framework correlate well with bench test results.
- The design strategy of the present ATR blade prove to be appropriate by confirming the actuation capability and structural integrity exhibited by the prototype blade and the modified test blades.

and the experimental data acquired in the amplitude of the fixed- and rotating-system loads. Since the discrepancy is considered to result from the less sophisticated aerodynamics model adopted, analysis with more sophisticated model is recommended.

- The discrepancy in the in the amplitude of the fixed- and rotating-system loads also results from incomplete representation of the structural components existing in the testing apparatus. Thus, further dynamic characterization of the ARES testbed is recommended.

- System identification and closed-loop controller design was conducted based on the established analytical model due to the limited availability of the experimental data. However, in order to apply a closed-loop controller in the practical system, experimental data is recommended for final tuning of the controller.

- Further improvement of the vibration reduction capability through optimization study of the active blade design parameters is suggested. This includes tailoring of active and passive plies included in blade lay-up, sizing of the active region, etc. Basic dynamic characteristics of the blade such as the natural frequencies may be another influencing factor for control authority in specific frequencies.

- It is desirable to use the concept of integral blade twist actuation as a means of acoustic noise reduction for the rotor system. In order to analyze the active rotor system for such purpose, more refined aerodynamics model is required to accurately predict the pressure distribution around the blades in a specific flight condition. For a wind-tunnel experiment, quiet environments are required so that the reliable acoustic data may be collected. A noise-reducing closed-loop controller can be designed and tested by conducting the procedures suggested in this thesis.

Appendix A

State-space Formulation for Hover Analysis

Explicit expressions of the state space representation for hover analysis, Eq. (2.32), are provided. Since detailed expressions of the sub-matrices included in the matrices **E** and **A** in Eq. (2.33) are found in the appendices of [63], non-zero sub-matrices in the matrix **B** are only described in this section.

$$
\begin{aligned}
\frac{\partial F_S}{\partial V} &= \sum_i \left(\frac{\partial F_S}{\partial V}\right)_i \\
\left(\frac{\partial F_S}{\partial V}\right)_i &= \left[\frac{\partial f_{u_i}}{\partial V} \;\; \frac{\partial f_{\psi_i}}{\partial V} \;\; \frac{\partial f_{F_i}}{\partial V} \;\; \frac{\partial f_{M_i}}{\partial V} \;\; \frac{\partial f_{P_i}}{\partial V} \;\; \frac{\partial f_{H_i}}{\partial V} \;\; \frac{\partial f_{u_j}}{\partial V} \;\; \frac{\partial f_{\psi_j}}{\partial V} \;\; \frac{\partial f_{F_j}}{\partial V} \;\; \frac{\partial f_{M_j}}{\partial V}\right]^T \\
\frac{\partial f_{u_i}}{\partial V} &= 0 \\
\frac{\partial f_{\psi_i}}{\partial V} &= -\frac{\Delta l_i}{2} C^T C^{ab} (r \widetilde{F_{B_i}^{(a)}} + t M_{B_i}^{(a)}) F_i \\
\frac{\partial f_{F_i}}{\partial V} &= -\frac{\Delta l_i}{2} C^T C^{ab} (r F_{B_i}^{(a)} + t M_{B_i}^{(a)}) \\
\frac{\partial f_{M_i}}{\partial V} &= -\frac{\Delta l_i}{2} \left(\Delta + \frac{\tilde{\theta}_i}{2} + \frac{\theta_i \theta_i^T}{4}\right) C^{ab} (t F_{B_i}^{(a)} + s M_{B_i}^{(a)}) \\
\frac{\partial f_{P_i}}{\partial V} &= 0 \\
\frac{\partial f_{H_i}}{\partial V} &= 0 \\
\frac{\partial f_{u_j}}{\partial V} &= 0
\end{aligned}
$$

Appendix B

Time Integration Formulation for Forward Flight Analysis

The energy decaying time integration of the beam formulation mentioned in Section 2.5.2 is summarized as follows. The displacement-based form of beam formulation, Eq. (2.22), can be expressed conveniently as

$$(\mathbf{R}\mathbf{p}_B)^{\bullet} + \mathbf{U}[\tilde{\widetilde{u}}]\mathbf{R}\mathbf{p}_B - (\mathbf{R}\mathbf{f}_B)' - \mathbf{U}[\widetilde{u_o'} + \tilde{\widetilde{u}}']\mathbf{R}\mathbf{f}_B = \mathbf{q} \tag{B.1}$$

where

$$\mathbf{R} = \begin{bmatrix} C^{Bb}C^{ba} & 0 \\ 0 & C^{Bb}C^{ba} \end{bmatrix}$$

$$\mathbf{U}[.] = \begin{bmatrix} 0 & 0 \\ [.] & 0 \end{bmatrix}$$

Note that $\mathbf{q}$ in Eq. (B.1) now represents all the terms including the actuation forces at the right hand side of Eq. (2.21). A time discretization scheme can be applied first over the time step, from t_n^- to t_{n+1}^-:

$$\frac{\mathbf{R}_{n+1}^- \mathbf{p}_{Bn+1}^- - \mathbf{R}_n^- \mathbf{p}_{Bn}^-}{\Delta t} + \mathbf{U}\left[\frac{\widetilde{u_{n+1}^-} - \widetilde{u_n^-}}{\Delta t}\mathbf{G}_m\right]\frac{\mathbf{p}_{Bn}^- + \mathbf{p}_{Bn+1}^+}{2} \tag{B.2}$$

Appendix C

AFC Distribution in the ATR Prototype Blade

The following table presents the electromechanical coupling coefficients (d_{11} and d_{12}) of the individual AFC packs embedded in the ATR prototype blade along its spanwise location. It is noted that the distribution of the packs is designed so that those with the best performance can be located at the inboard of the blade and the performance difference between top and bottom surfaces at the same spanwise location is to be minimized.

Appendix D

Material Properties of the ATR Test Blade Constituents

The following two tables present the material properties of the constituent materials used in the ATR test blades manufacturing.

Table D.1: Material properties of the constituents in the ATR test blades

	E-Glass fabric	**EA9628 adhesive**	**Rohacell foam spar**	**Rohacell foam fairing**
Thickness (μm)	114.3	101.6	-	-
Density (kg/m^3)	1,716	1,163	75	35
E_L (GPa)	19.3	2.38	0.0896	0.035
G_{LT} (GPa)	4.14	0.69	0.0296	0.0138
	Fiber glass uni-tape	**Flexible circuit**	**Front ballast weight (tungsten)**	**Strain gauge wires**
Dimension	thickness	width	diameter	diameter
	203.2 μm	6.604 mm	4.7625 mm	40×0.381 mm
Density (kg/m^3)	1,799	3,044	19,100	8,900
E_L (GPa)	48.2	-	-	-
G_{LT} (GPa)	5.7	-	-	-

Appendix E

LTP System and its Identification

What follows is a summary of the identification technique for LTP systems presented in [62].

E.1 Characteristics of LTP system

Linear time periodic system can be represented in a state-space form as

$$\begin{aligned} \dot{x}(t) &= A(t)x(t) + B(t)u(t) \\ y(t) &= C(t)x(t) + D(t)u(t) \end{aligned} \tag{E.1}$$

where the matrices $A(t)$, $B(t)$, $C(t)$, and $D(t)$ are in general periodic, with period T. When a sinusoidal signal excites an LTP system, the system responds with the superposition of sinusoids not only of the input frequency ω, but also of several other frequencies, $\omega + n\omega_p$, each with its own amplitude and phase, where n is an integer, and ω_p is the system major frequency, given as

$$\omega_p = 2\pi/T \tag{E.2}$$

The frequencies $\omega + n\omega_p$ are shifted harmonics, and they are often referred to simply as "harmonics."

terms of their Fourier series, and using the harmonic balance approach, one obtains

$$\begin{aligned} s_n x_n &= \sum_{m\in Z} A_{n-m}x_m + \sum_{m\in Z} A_{n-m}u_m \\ y_n &= \sum_{m\in Z} C_{n-m}x_m + \sum_{m\in Z} D_{n-m}u_m \end{aligned} \tag{E.8}$$

The summations in the previous expression, Eq. (E.8), can be transformed into matrix form as

$$\begin{aligned} s\mathcal{X} &= (\mathcal{A}-\mathcal{N})\mathcal{X} + \mathcal{B}\mathcal{U} \\ \mathcal{Y} &= \mathcal{C}\mathcal{X} + \mathcal{D}\mathcal{U} \end{aligned} \tag{E.9}$$

The updated state vector $\mathcal{X}$ in Eq. (E.9) represents the original ones at various harmonics of the system major frequency as

$$\mathcal{X} = \begin{bmatrix} \vdots \\ x_{-2} \\ x_{-1} \\ x_0 \\ x_1 \\ x_2 \\ \vdots \end{bmatrix} . \tag{E.10}$$

The updated system dynamics matrix $\mathcal{A}$ in Eq. (E.9) is a doubly-infinite Toeplitz matrix given by

$$\mathcal{A} = \begin{bmatrix} \ddots & \vdots & \vdots & \vdots & \\ \cdots & A_0 & A_{-1} & A_{-2} & \cdots \\ \cdots & A_1 & A_0 & A_{-1} & \cdots \\ \cdots & A_2 & A_1 & A_0 & \cdots \\ & \vdots & \vdots & \vdots & \ddots \end{bmatrix} \tag{E.11}$$

where the submatrix A_n represents the n-th Fourier coefficient of $A(t)$. $\mathcal{B}$, $\mathcal{C}$, and $\mathcal{D}$ can be defined in the similar manner. The frequency modulation matrix $\mathcal{N}$ is an

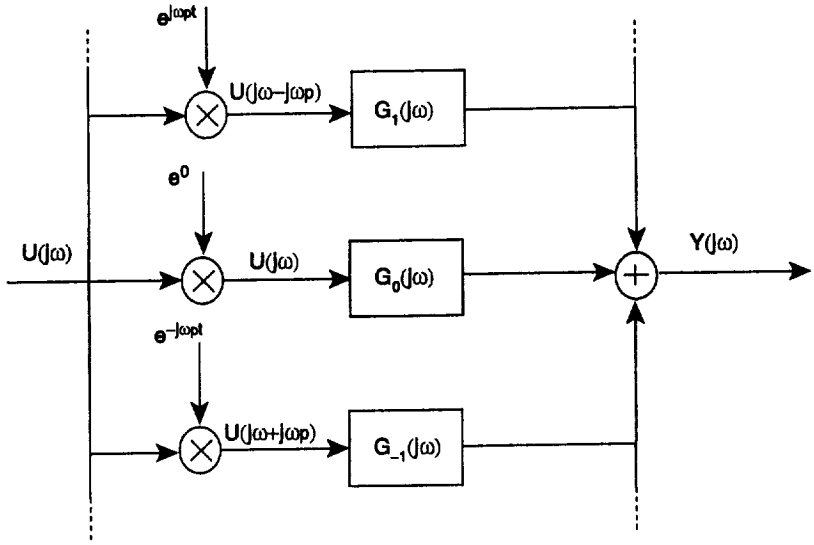

Figure E-1: LTP system block diagram with three transfer functions [62]

G_1, and G_{-1}, respectively. Thus,

$$Y(j\omega) = G_0(j\omega)U(j\omega) + G_1(j\omega)U(j\omega - j\omega_p) + G_{-1}(j\omega)U(j\omega + j\omega_p) \qquad \text{(E.14)}$$

In time domain, Eq. (E.14) can be expressed using the convolution as follows

$$y(t) = g_0(t) * u(t) + g_1(t) * [u(t)e^{j\omega_p t}] + g_{-1}(t) * [u(t)e^{-j\omega_p t}] \qquad \text{(E.15)}$$

A linear system represented by both Eqs. (E.14) and (E.15) is depicted in the block diagram in Fig. E-1.

However, since there is only one equation available in order to estimate three transfer functions G_0, G_1, and G_{-1}, the identification problem becomes underdetermined. This leads to the need of three different input applications for composing three independent equations, each of which is similar to Eq. (E.14). Due to the periodic nature of the system under consideration, it is extremely important to account for the time of application of each input relative to the system period T. In order for the system behavior to be completely analyzed, multiple identical input signals are applied which are evenly located over the system period. In Fig. E-2, an example of the input signals are shown. There, three input signals are created in sine-sweep

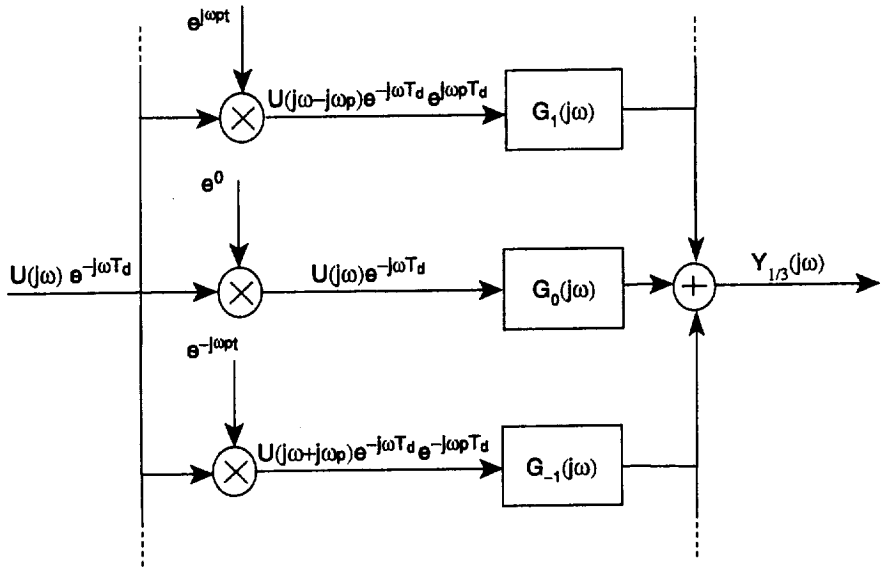

Figure E-3: Delayed input signal and corresponding output of LTP system [62]

Then, Eq. (E.17) becomes

$$\begin{Bmatrix} Y_0 \\ Y_{1/3} \\ Y_{2/3} \end{Bmatrix} = \begin{bmatrix} U(j\omega) & U(j\omega - j\omega_p) & U(j\omega + j\omega_p) \\ U(j\omega) & U(j\omega - j\omega_p)W & U(j\omega + j\omega_p)W^{-1} \\ U(j\omega) & U(j\omega - j\omega_p)W^2 & U(j\omega + j\omega_p)W^{-2} \end{bmatrix} \begin{Bmatrix} G_0 \\ G_1 \\ G_{-1} \end{Bmatrix} \tag{E.19}$$

When the W terms are separated, Eq. (E.19) becomes

$$\underbrace{\begin{Bmatrix} Y_0 \\ Y_{1/3} \\ Y_{2/3} \end{Bmatrix}}_{Y} = \underbrace{\begin{bmatrix} 1 & 1 & 1 \\ 1 & W & W^2 \\ 1 & W^2 & W^4 \end{bmatrix} \begin{bmatrix} U(j\omega) & 0 & 0 \\ 0 & U(j\omega - j\omega_p) & 0 \\ 0 & 0 & U(j\omega + j\omega_p) \end{bmatrix}}_{U} \underbrace{\begin{Bmatrix} G_0 \\ G_1 \\ G_{-1} \end{Bmatrix}}_{G} \tag{E.20}$$

Notice that the first matrix multiplied to give U in Eq. (E.20) is the one that commonly arises in discrete Fourier transform. Eq. (E.20) can be simply written as

$$Y = UG \tag{E.21}$$

$\mathbf{y}$ and ψ are similarly defined. If the transfer functions of the system as many as n_h need to be identified, an $n_h \times n$ matrix $\mathbf{U}$ is constructed according to Eq. (E.20) with an appropriately modulated and Fourier transformed vector $\mathbf{u}$ at each row, so that

$$\mathbf{U} = \begin{bmatrix} \mathcal{F}\{[e^{mj\psi_1}u_1 & \dots & \dots & e^{mj\psi_n}u_n]\} \\ \vdots & & \vdots & \vdots \\ \mathcal{F}\{[e^{1j\psi_1}u_1 & \dots & \dots & e^{1j\psi_n}u_n]\} \\ \mathcal{F}\{[e^{0j\psi_1}u_1 & \dots & \dots & e^{0j\psi_n}u_n]\} \\ \mathcal{F}\{[e^{-1j\psi_1}u_1 & \dots & \dots & e^{-1j\psi_n}u_n]\} \\ \vdots & & \vdots & \vdots \\ \mathcal{F}\{[e^{-mj\psi_1}u_1 & \dots & \dots & e^{-mj\psi_n}u_n]\} \end{bmatrix} \tag{E.24}$$

where $m = \frac{n_h - 1}{2}$. Eq. (E.24) can be described in a more compact notation as

$$\mathbf{U} = \begin{bmatrix} \mathbf{u}(\omega - m\omega_p) & \dots & \mathbf{u}(\omega - \omega_p) & \mathbf{u}(\omega) & \mathbf{u}(\omega + \omega_p) & \dots & \mathbf{u}(\omega + m\omega_p) \end{bmatrix}^T \tag{E.25}$$

Similarly, $\mathbf{Y}$ can be constructed as the discrete Fourier transform of the vector $\mathbf{y}$ as

$$\mathbf{Y} = \mathcal{F}\left\{\begin{bmatrix} y_1 & y_2 & y_3 & \dots & y_n \end{bmatrix}\right\} \tag{E.26}$$

Recalling that the empirical transfer function estimate (ETFE) of a linear time invariant (LTI) system involves the power and cross spectral densities of input and output, these spectral densities can be defined in a similar manner for the present LTP system as

$$\begin{aligned} \mathbf{\Phi_{UU}} &= \mathbf{U}^{*T}\mathbf{U} \\ \mathbf{\Phi_{UY}} &= \mathbf{U}^{*T}\mathbf{Y} \end{aligned} \tag{E.27}$$

curvature of the transfer functions, so that

$$J = \min \left[(\mathbf{Y} - \mathbf{U}^T \widehat{\mathbf{G}})^2 + \alpha (\mathbf{D}^2 \widehat{\mathbf{G}})^2 \right] \tag{E.32}$$

where $\mathbf{D}^2$ is a second-order difference operator, and α is a weighting factor. By taking the derivative of J with respect to $\widehat{\mathbf{G}}$ in Eq. (E.32) and setting it to zero, the minimizing $\widehat{\mathbf{G}}$ can be found as

$$\widehat{\mathbf{G}} = \left[\mathbf{U}^T \mathbf{U} + \alpha \mathbf{D}^4 \right]^{-1} \mathbf{U}^T \mathbf{Y} \tag{E.33}$$

where $\mathbf{D}^4 = \mathbf{D}^2 \cdot \mathbf{D}^2$. Eq. (E.33) is the final form that is utilized in the following system identification, and more issues on the practical implementation of Eq. (E.33) and solutions are provided in [62].

Bibliography

[1] E. M. Laing. Army helicopter and vibration survey mehtods and results. *Journal of the American Helicopter Society*, 19(3):28–38, 1974.

[2] W. E. Hooper. Vibratatory airloading of helicopter rotors. *Vertica*, 8(2):73–92, 1984.

[3] W. K. Wilkie. *Anisotropic Piezoelectric Twist Actuation of Helicopter Rotor Blades: Aeroelastic Analysis and Design Optimization.* PhD dissertation, University of Colorado, Department of Aerospace Engineering Sciences, December 1997.

[4] R. G. Loewy. Helicopter vibrations: A technological perspective. *Journal of the American Helicopter Society*, 29(4):4–30, 1984.

[5] R. Bielawa. *Rotary Wing Structural Dynamics and Aeroelasticity.* American Institute of Aeronautics and Astronautics, 1992.

[6] B. Wang, L. Kitis, W. Pilkey, and A. Palazzolo. Helicopter vibration reduction by local structural modification. *Journal of the American Helicopter Society*, 27(3):43–47, 1982.

[7] M. Hamouda and G. Pierce. Helicopter vibration suppression using simple pendulum absorbers on the rotor blade. *Journal of the American Helicopter Society*, 29(3):19–29, 1984.

[8] J. A. Molusis, Hammond C. E., and Cline J. H. A unified approach to the optimal

[17] R. G. Loewy. Recent developments in smart structures with aeronautical applications. In *Proceedings of the 37th Israel Annual Conference on Aerospace Sciences*, February 26–27 1997.

[18] P. P. Friedmann. The promise of adaptive materials for alleviating aeroelastic problems and some concerns. In *Proceedings of Innovation in Rotorcraft Technology*, pages 10.1–10.16, London, United Kingdom, June 24–25 1997. Royal Aeronautical Society.

[19] I. Chopra. Status of application of smart structures technology to rotorcraft systems. *Journal of the American Helicopter Society*, 45(4):228–252, 2000.

[20] V. Giurgiutiu. Recent advances in smart-material rotor control actuation. In *Proceedings of the AIAA/ASME/ASCE/AHS/ASC 41st Structures, Structural Dynamics and Materials Conference- Adaptive Structures Forum*, Atlanta, Georgia, April 3–6 2000. AIAA Paper No. 2000–1709.

[21] T. A. Millott and P. P. Friedmann. Vibration reduction in helicopter rotors using an actively controlled partial span trailing edge flap located on the blade. NASA-CR-4611, June 1994.

[22] R. L. Jr. Spangler and S. R. Hall. Piezoelectric actuators for helicopter rotor control. SSL Report 1-89, SERC 14-90, MIT Space Engineering Research Center, Massachusetts Institute of Technology, Cambridge, Massachusetts, January 1989.

[23] C. Walz and I. Chopra. Design, fabrication and testing of a helicopter rotor model with smart trailing edge flaps. In *Proceedings of the AIAA/ASME/ASCE/AHS/ASC 35th Structures, Structural Dynamics and Materials Conference- Adaptive Structures Forum*, Hilton Head, SC, April 21-22 1994. AIAA-94-1767-CP.

[24] M. V. Fulton and R. Ormiston. Hover testing of a small-scale rotor with on-blade elevons. In *Proceedings of the American Helicopter Society 53rd Annual Forum*, Virginia Beach, VA, April 29-May 1 1997.

blade. In *Proceedings of the American Helicopter Society 55th Annual Forum*, Montreal, Canada, May 25–27 1999.

[34] A. A. Bent and N. W. Hagood. Piezoelectric fiber composites with interdigitated electrodes. *Journal of Intelligent Material Systems and Structures*, 8:903–919, 1997.

[35] J. P. Rodgers, A. A. Bent, and N. W. Hagood. Characterization of interdigitated electrode piezoelectric fiber composites under high electrical and mechanical loading. In *Proceedings of the Society of Photo-Optical and Instrumentation Engineers*, San Diego, California, 1996.

[36] K. W. Wilkie, R. G. Bryant, J. W. High, R. L. Fox, R. F. Hellbaum, Jr. A. Jalink, B. D. Little, and P. H. Mirick. Low-cost piezocomposite actuator for structural control applications. In *Proceedings of SPIE Smart Structures and Materials Conference*, Newport Beach, CA, March 5–9 2000.

[37] P. C. Chen and I. Chopra. A feasibility study to build a smart rotor: Induced-strain actuation of airfoil twisting using piezoceramic crystals. In *Proceedings of the Society of Photo-Optical and Instrumentation Engineers*, pages 238–254, San Diego, California, Vol. 1917 1993.

[38] R. C. Derham, B. Matthew, and D. B. Weems. An introduction to the aeromechanical design space of "smart" rotors. In *Proceedings of American Helicopter Society Northeast Region National Specialists' Meeting–Improving Rotorcraft Acceptance through Active Controls Technology*, Bridgeport, CT, October 4–5 2000.

[39] A. J. duPlessis and N. W. Hagood. Modeling and experimental testing of twist actuated single cell composite beams for helicopter blade control. AMSL 96-1, Massachusetts Institute of Technology, February 1996.

[40] W. K. Wilkie, M. L. Wilbur, P. H. Mirick, C. E. S. Cesnik, and S.-J. Shin. Aeroelastic analysis of the NASA/ARMY/MIT active twist rotor. In *Proceedings*

[49] M. L. Wilbur, P. H. Mirick, Jr. W. T. Yeager, C. W. Langston, C. E. S. Cesnik, and S.-J. Shin. Vibratory loads reduction testing of the NASA/ARMY/MIT active twist rotor. In *Proceedings of the American Helicopter Society 57th Annual Forum*, Washington, DC, May 9–11 2001.

[50] D. A. Peters and C. J. He. A closed form unsteady aerodynamic theory for lifting rotor in hover and forward flight. In *Proceedings of the American Helicopter Society 43rd Annual Forum*, St. Louis, Missouri, May 1987.

[51] O. A. Bauchau. Computational schemes for flexible, nonlinear multi-body systems. *Multibody System Dynamics*, 2:169–225, 1998.

[52] C. E. S. Cesnik and M. Ortega-Morales. Active composite beam cross-sectional modeling-stiffness and active force components. In *Proceedings of the 40th AIAA Structures, Structural Dynamics, and Materials Conference*, St. Louis, Missouri, April 20–23 1999. AIAA Paper No. 99–1548.

[53] V. K. Wickramasinghe and N. W. Hagood. Material characterization of active fiber composite actuators for active twist helicopter rotor blade applications. In *Proceedings of the AIAA/ASME/ASCE/AHS/ASC 41st Structures, Structural Dynamics and Materials Conference- Adaptive Structures Forum*, Atlanta, Georgia, April 3–6 2000. AIAA Paper No. 2000–1499.

[54] X. Shang and D. H. Hodges. Aeroelastic stability of composite rotor blades in hover. In *Proceedings of the 36th Structures, Structural Dynamics and Materials Conference*, New Orleans, Louisiana, April 10 – 12 1995.

[55] D. H. Hodges, A. R. Atilgan, C. E. S. Cesnik, and M. V. Fulton. On a simplified strain energy function for geometrically nonlinear behavior of anisotropic beams. *Composites Engineering*, 2(5 – 7):513 – 526, 1992.

[56] D. A. Peters and C. J. He. Finite state induced flow models part II: Three-dimensional rotor disk. *Journal of Aircraft*, 32(2):323–333, 1995.

Biographical Note

SangJoon Shin graduated from Seoul National University in Seoul, Korea with a B.S. degree in Aerospace Engineering in February, 1989, with honors. He received a M.S. degree in the same field at Seoul National University in February, 1991. In 1991, he joined the Korean Agency for Defense Development in Taejon, Korea as a research engineer. He had five years' experience at the Helicopter Systems Department and the Turboprop Trainer Systems Group. In August, 1996, he came to the United States and joined the graduate program of the Aeronautics and Astronautics at Massachusetts Institute of Technology. He received the second Science Master degree in Aeronautics and Astronautics in June, 1999. His thesis was entitled: "Design, Manufacturing, and Testing of an Active Twist Rotor." He continued the research of the active helicopter rotor for his doctoral degree.